Investigation of Heavy Quark and Multiple Interactions at HERA.

by
Lluís Martí Magro
aus Barcelona.

Diplomarbeit
äquivalente Schrift

Hamburg, 2005.

Contents

Chapter 1

Introduction.

This thesis is oriented to the study of heavy quark photoproduction and multiple interactions, MI. For this reason we search for D^* Mesons, in order to tag the charm quark, and we restrict ourselves in the region: $Q^2 < 1\ GeV^2$. For the theoretical calculations we use two Monte Carlo event generators: Rapgap 3.1 [1] and Pythia 6.2 [2].

Heavy quark production provide a large hard scale and therefore a small α_s, which allows to test the perturbative QCD theory. On the other hand, MI has been proven to be important in hadron-hadron collisions. In this thesis, using MC event generators, we search for possible signals of MI in heavy quark production in electron-proton, *ep*, collisions.

The thesis begins with a Theoretical Overview, with an introduction to *ep* collisions physics and the heavy quark photoproduction. We also give an introduction to the MI model included in Pythia. The next chapter introduces the concept of jet and presents some methods for the Heavy Quark Identification. After these two theoretical chapters there is a study of the direct and photon resolved processes, as well as the parton showering with Rapgap. Since this thesis is oriented to the study of MI, Pythia plays a very important role because it includes a MI model also for *ep* collisions. Therefore, the fourth chapter is oriented to study the different steps in the event generation in Pythia. Chapter 7 is a D^* Meson photoproduction study, where we include a comparison between the data, taken from the PhD Thesis of Gero Flucke [3]. Finally, chapter 8 is a search for possible signals on MI. In hadron-hadron collisions it is clear that MI play a role. In *ep* collisions

it is not so clear although MI could play a role in resolved photon events. The aim of this chapter is to find signals where HERA measurements could be sensitive to MI.

A general table with the most important general parameters for RAPGAP and PYTHIA can be found in appendix A.

Chapter 2

Theoretical Overview

In this chapter we give an introduction to the physics of Heavy Quarks, HQ, at HERA. We begin with a general introduction to eletron-proton, *ep*, physics and then we describe in more detail photoproduction of HQ, the parton evolution and parton showers, PS. After that we describe multiple interaction, MI, processes.

2.1 *ep* Scattering.

In a high energy *ep* collider like HERA the aim is to study the basic interactions in nature and the structure of the proton. The center-of-mass energy, $\sqrt{s}$, is defined by:

$$s = (P_e + P)^2 \tag{2.1}$$

where P_e and P are the incoming electron and the proton 4-momentum respectively. The role of the electron is to "illuminate" the inner parts of the proton. Such collisons are classified as elastic or inelastic. In elastic collisions the proton survives the collision with the electron and does not break up. Figure 2.1 shows the lowest-order *ep* elastic transition:

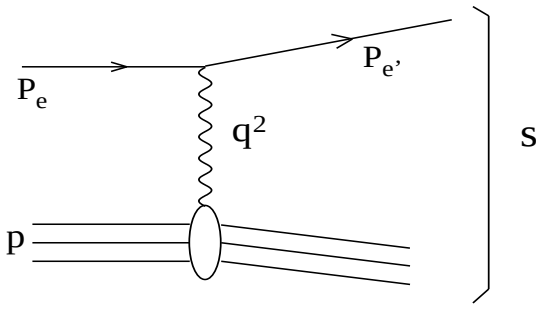

Figure 2.1: *Elastic ep collision.*

where the squared 4-momentum transfer, q, is defined by:

$$q^2 = (P_e - P_{e'})^2 \tag{2.2}$$

and $P_{e'}$ is the scattered electron 4-momentum.

In order to deal with a positive defined variable we define the virtuallity $Q^2 = -q^2$. Only with elastic collisions we are not able to look at the structure of the proton, so what we do is to increase Q^2 to acquire a better spatial resolution in the proton. Increasing Q^2 the probability of the proton to break up also increases and then we have a more complicated picture, see figure 2.2.

These collisions, $e + p \rightarrow e + X$, are called inelastic ep collisions and are characterized by a hadronic invariant mass, W, defined as:

$$W^2 = (P + q)^2 \tag{2.3}$$

such that in inelastic ep collisions the condition: $W^2 \gg M^2$ is fulfilled with M being the proton mass. This condition actually defines inelastic collisions and can be given both for small and large values of Q^2.

It is useful to define the pseudo-rapidity, η, the fraction of the proton momentum carried by a parton from the proton, x, and y, the fraction of the electron energy carried by the photon (in the proton rest frame):

$$\eta = -\ln\left(\tan\frac{\theta}{2}\right) \tag{2.4}$$

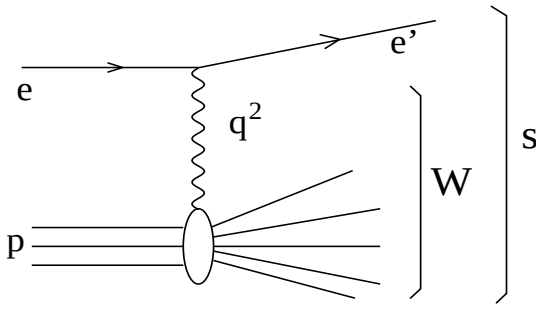

Figure 2.2: *Inelastic ep collision.*

$$x = \frac{Q^2}{2\ P \cdot q} \tag{2.5}$$

$$y = \frac{P \cdot q}{P \cdot P_e} \tag{2.6}$$

$$Q^2 = x \cdot y \cdot s \tag{2.7}$$

$$W^2 = y\ x - Q^2 = \frac{Q^2}{x}(1-x) \tag{2.8}$$

where θ is the polar angle where the incoming proton beam direction defines the positive z-axis. In equations(2.7) and (2.8) we neglected both the electron and the proton rest masses.

The cross section for the $e + p \rightarrow e + X$ process can be calculated in Quantum Electrodynamics, QED:

$$\frac{d^2\sigma}{dx\ dy} = \frac{2\ \pi\ \alpha_{em}^2}{Q^4}\ s\ \left(2\ F_1(x)\ x\ y^2 + 2\ F_2(x)\ (1-y)\right) \tag{2.9}$$

where α_{em} is the electromagnetic coupling constant, and F_1 and F_2 are structure functions. These structure functions contain our lack of knowledge on the proton structure, and cannot be calculated from first principles and have to be determined experimentally. We restrict to QED processes for $Q^2 < 1000\ GeV^2$ because, in this case, weak interactions are negligible due to the large masses of Z^0 and $W^{\pm}$.

In the Quark Parton Modell, QPM, the quarks in the proton are considered as free particles and the scattering process can be viewed as an elastic eletron-quark scattering, see figure 2.3.

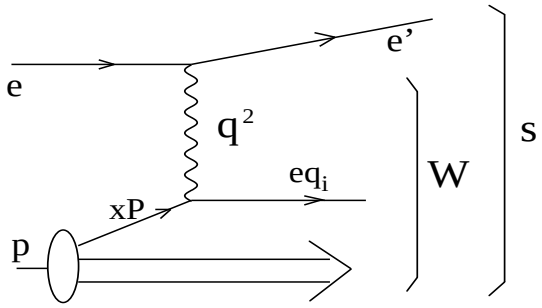

Figure 2.3: *Electron-proton collision in the QPM model. The quark is viewed as free particle and the photon-quark collision is elastic.*

In this model we have the momentum sum rule:

$$\sum_i \int_0^1 x\ f_i\left(x\right) dx = 1 \tag{2.10}$$

where the sum runs over all the quarks in the proton, i, and $f_i\left(x\right)$ are the parton densities. Then $f_i\left(x\right) dx$ represents the probability of finding a quark i with a momentum fraction between $(x, x + dx)$. Since quarks are $\frac{1}{2}$ spin particles, the differential cross section of such a process, $e + q \rightarrow e + q$, is:

$$\frac{d\hat{\sigma}}{dy} = e_{q_i}^2\ \frac{2\ \pi\ \alpha^2}{Q^4}\ \hat{s}\ \left(1 + (1 + y)^2\right) \tag{2.11}$$

where e_{q_i} is the scattered-quark charge and $\hat{s}$ is the center-of-mass energy of the quark-electron subprocess. If we sum over all the quarks and integrate over x':

$$\frac{d^2\sigma}{dx\ dy} = \int_0^1 \sum_i \frac{d\hat{\sigma}}{dy}\ x'\ f_i\left(x'\right) \delta(x - x') dx' =$$

$$\frac{2\ \pi\ \alpha^2}{Q^4}\ s\ \left(1 + (1 + y)^2\right) \sum_i e_{q_i}^2\ x\ f_i\left(x\right) \tag{2.12}$$

If now we compare equations 2.9 and 2.12 we find that the QPM predicts:

$$F_2(x) = \sum_i e_{q_i}^2 \; x \; f_i(x) \tag{2.13}$$

$$F_2(x) = 2 \; x \; F_1(x) \tag{2.14}$$

These are the Gallan-Gross relations

Experimentally it was shown that the quarks in the proton only carry 50% of the total momentum of the proton. The eq(2.10) does not hold as we postulated and the sum has to be extended to all the partons in the proton since the remainig 50% is carried by gluons and means a violation of the QPM as we formulated it. This is true particularly for very small x values, since the gluon density functions dominate over the quarks and QPM does not take into account processes like $\gamma^* q \to qg$ or $\gamma^* g \to q\bar{q}$. This is done by Quantum Chromodynamics, QCD. In pertubative QCD, pQCD, this can be calculated:

$$d\sigma \Big|_{ep \to eX} = \sum_i \int f_i\left(x, \mu_f^2\right) \; d\hat{\sigma}_i\left(\hat{s}, \alpha_s(\mu_r^2), \mu_r, \mu_f\right) \; dx \tag{2.15}$$

If we have a parton density function, $f_i\left(x, \mu_f^2\right)$, at a given scale, μ_f, then QCD predicts the parton density function at another scale via DGLAP (see section 2.3).

The QCD theory explains how the partons introduced in this chapter, quarks and gluons which are coloured particles, interact by exchanging a gluon, the quanta of the color field of the strong force. This theory is similar with QED but with important differences. In QCD we have nine gluons, bicolored states, carrying the strong force, whereas in QED we have only the photon. In QCD two gluons can interact with each other since they are coloured particles, whereas two photons do not interact because they do not carry electric charge. This last feature is very important and has deep consequences (the *asymptotic freedom*), rise of F_2 at small x and saturation effects.

2.2 Photoproduction regime and Heavy Quark production.

At HERA, the production of HQ is limited to charm and beauty flavours. The masses are large, larger than 1 GeV, in contrast to the light quark masses, about a few MeV. These provide a large hard scale to be used in pQCD due to their large masses which makes α_s small ($\alpha_s < 1$). This means that working with HQ is a good opportunity to test details in pQCD. All this features lead to a nice opportunity to study both the γq and gq couplings.

In photoproduction the photon is almost real and the virtuality, Q^2, is very small. This occurs if the scattering angle of the electron, θ, is small. This case, approximated by $Q^2 < 1\ GeV^2$, dominate the total ep cross section, as can be seen from eq(2.9).

In this case, the photon can fluctuate into a quark-antiquark pair and interact with the proton. In figure 2.4 are shown the leading order α_s diagrams in HQ photoproduction. In figure 2.4b) and c) is represented the resolved photon in two quarks, one of them interacting with the incoming gluon from the proton, emiting another gluon or being scattered respectively. In a similar way as in eq(2.15) the cross section for photoproduction is expressed:

$$\left.\frac{d^2\sigma}{dx_p dx_\gamma}\right|_{\gamma p} = \sum_{i,j} f_{i/p}\left(x_p, \mu_f^2\right) f_{j/\gamma}\left(x_\gamma, \nu_f^2\right) d\hat{\sigma}_{ij}\left(\hat{s}, \alpha_s(\mu_r^2), \mu_r, \mu_f, \nu_f\right) \quad (2.16)$$

where x_γ is the momentum fraction of the photon entering in the hard interaction. Here, the cross section is assumed to factorise into cross sections $\hat{\sigma}_{ij}$, which describe the interaction between the partons i from the proton and the partons j from the resolved photon, and the parton density distributions. We need therefore $f_{j/\gamma}$ and ν_f, and as before $f_{i/p}$ and μ_f, the parton densities and the factorisation scales in the proton and in the photon, respectively. An approximate measure using jets of x_γ is given by[1]:

$$x_\gamma = \frac{E_t^{Jet_1} e^{-\eta^{Jet_1}} + E_t^{Jet_2} e^{-\eta^{Jet_2}}}{2yE_e} \quad (2.17)$$

[1]The derivation is done in appendix B.

where the jet definition will be given in section 3.1, Jet_1 and Jet_2 are jets from the hard scattering, and E_t^{Jet} is the transverse energy of the jet, which is defined as:

$$E_t^{Jet} = \sqrt{(P_t^{Jet})^2 + m_{Jet}^2} = \sqrt{E_{Jet}^2 - P_z^{Jet}} \tag{2.18}$$

In direct processes, represented in figure 2.4a), the photon interacts as a whole with the incoming gluon and therefore x_γ is equal to 1. The parton j is just the photon and we can take $f_{j/\gamma}$ as $\delta(x_\gamma - 1)$ in eq(2.16) taking the appropriate $\hat{\sigma}_{ij}$.

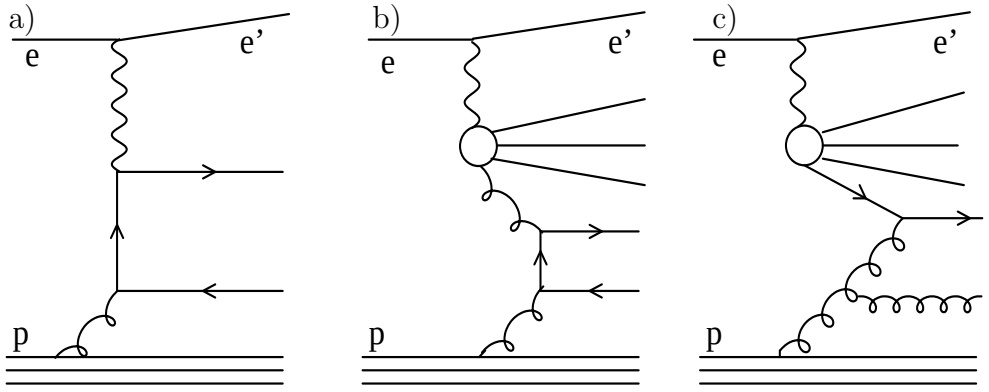

Figure 2.4: *Leading order processes: direct a), resolved photon b) and heavy quark excitation c).*

Other contributions come from resolved processes, where a gluon from the proton scatters a charm quark from the resolved photon, i.e. heavy quark production, this is called charm excitation. This contribution is quite large and cannot be neglected.

2.3 Parton evolution and Parton Shower.

In section 2.1 we introduced the parton density functions, $f_i\left(x, \mu_f^2\right)$, which cannot be calculated from first principles. However, in pQCD the evolution of the parton density functions can be calculated from a scale μ_f to another scale μ, $\mu \neq \mu_f$ using the DGLAP evolution. In general, to be able to evolve

the incoming partons from the proton to the hard scattering we have three different approaches: DGLAP, BFKL and CCFM, which are briefly described below.

In this section we view a $2 \to n$ process as a factorisation of a hard scattering, where the hardest jets are usually created, and a parton evolution from the proton to the hard scattering, i.e. a sequence of branchings, starting from the proton and ending in the hard scattering, where the different approximations differ:

DGLAP (Dokshitzer, Gribov, Lipatov, Altarelli, Parisi). [2, 4]

In this approximation the parton coming from the proton evolves according to diagrams with leading contributions of $log\ Q^2$. This means there is a strong ordering in virtualities before entering in the hard scattering, where we find the largest virtuality. This virtuality grows from a virtuality q_0 up to its highest value q_n, such that in each branching i the condition: $q_{i-1} \ll q_i \ll q_{i+1}$ is fulfilled. This virtuality ordering, $q_0 \ll q_1 \ll ... \ll q_n$ leads to a strong ordering of the transverse momenta of the parton, k_t, in the evolution for small x: $k_{t,0} \ll k_{t,1} \ll ... \ll k_{t,n}$, where $k_t = \frac{q^2}{1-x}$. Since the virtuality of the hard scattering is much larger than the highest virtuality in the parton evolution, the virtuality of the parton entering in the hard scattering can be neglected. This means that the parton can be treated as collinear with the incoming proton and the partonic cross sections introduced in eq(2.15) can be calculated on-mass-shell. Figure 2.5 represents the parton evolution.

In each branching, i, the relevant kinematic variables are x_i and q_i. The differential probability for a parton a to branch into two partons bc is given by:

$$dP_a = \frac{\alpha_s}{2\ \pi}\ P_{a\to bc}(x)\ dtdx \tag{2.19}$$

where t is defined as:

$$t = \ln\frac{q^2}{\Lambda} \to dt = d\ln(q^2) = \frac{dq^2}{q^2} \tag{2.20}$$

where Λ is the QCD scale Λ_{QCD}. For each branching process, $q \to qg$, $g \to gg$, $g \to q\bar{q}$ the theory provides the appropriate *splitting kernel*, $P_{a\to bc}$, see for example [2, 4].

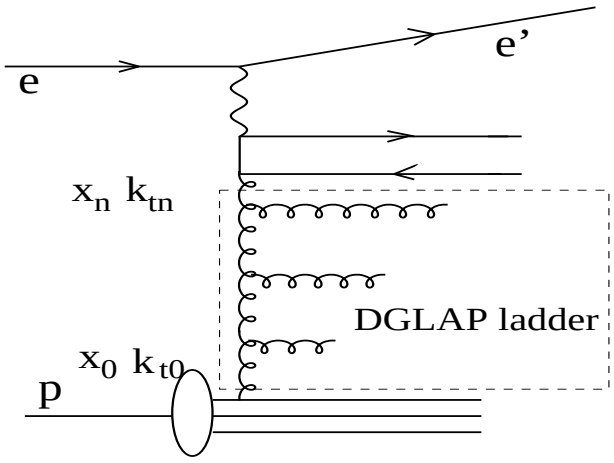

Figure 2.5: *DGLAP parton evolution. The ladder exhibits a strong ordering in the transverse momenta.*

Without taking into account the previous evolution, the probability of a parton to branch in a small interval of t, δt, is:

$$\Gamma_{a\to bc}(t)\ \delta t = \int_{x_-(t)}^{x_+(t)} \frac{\alpha_{abc}}{2\ \pi}\ P_{a\to bc}(x)\ dx\delta t \tag{2.21}$$

Then the probability for no branching is: $1-\sum_{bc}\Gamma_{a\to bc}(t)\ \delta t$ and therefore if we evolve from a virtuality t_0 to t, we have to take into account the diagrams in figure 2.6 to find the no-branching probability:

$$\Gamma_{a\to a}(t_0,t) = e^{-\int_{t_0}^{t}\ dt'\sum_{bc}\Gamma_{a\to bc}(t')} \tag{2.22}$$

In conclusion, the probability of branching at a virtuality t is:

$$\frac{dP_a}{dt} = e^{-\int_{t_0}^{t}\ dt'\sum_{bc}\Gamma_{a\to bc}(t')}\ \left(\sum_{bc}\Gamma_{a\to bc}(t)\right) \tag{2.23}$$

This is: the probability of no-branching from the starting virtuality t_0 to the virtuality, t (t_0 can be the initial virtuality or the last branching virtuality) multiplied by the probability of branching at the virtuality t. The exponential factor is the so called *Sudakov form factor*.

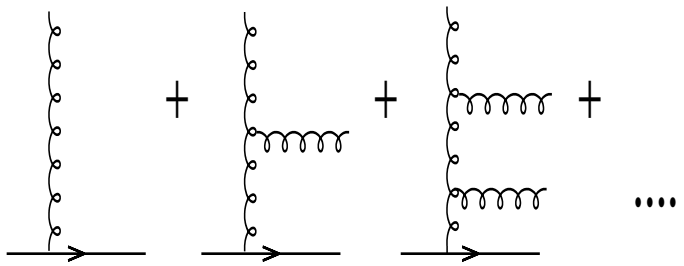

Figure 2.6: *Diagrams to be taken into account to calculate the no-branching probability for a parton going from a virtuality t_0 to another t.*

Note that all this machinery does not take into account if the virtuality ordering grows or decreases and therefore it can be used for the outgoing partons of the hard interaction as well as for the incoming partons to allow further parton showering. The parton evolution up to the hard scattering is called initial state PS, whereas the further branchings after the hard scattering are called final state PS. However, in MC programs the initial PS is treated in a "*backward evolution*" approach, where the parton densities are also included in the evolution process.

Monte Carlo event generators using DGLAP evolution have as parameters the maximum and minimum virtuality allowed in the parton shower and Λ_{QCD}. In chapter 6 we will see the effects of this parameter for heavy quark production using the event generator PYTHIA 6.2 [2].

DGLAP provides a good description of most of the processes at HERA, but this equation is expected to fail for low x processes where contributions from $log\ 1/x$ become as large as $log\ 1/Q^2$. An example would be forward jet production, where a better description of low x physics may be needed.

BFKL (Balitsky, Fadin, Kuraev, Lipatov). [5]

At large energies, i.e. small x ($W^2 \sim 1/x$), effects of finite tranverse momenta can be observed. In this approximation for asymptotically large energies, or small x, only leading contributions of $log\ 1/x$ are considered. We have therefore a strong ordering in the fractional momenta x: $x_0 \gg x_1 \gg ... \gg x_n$.

This approximation is valid in regions of small x where DGLAP is expected to fail. Since there is no virtuality ordering in this approximation k_t

can take any value and therefore the partonic cross sections in eq(2.15) have to consider the finite transverse momentum and are calculated off mass shell.

CCFM (Catani, Ciafaloni, Fiorani, Marchesini). [6–8]

CCFM provides a bridge between the DGLAP and BFKL approximations and is valid in both regions where DGLAP and BFKL can be applied. It is then clear that the partonic cross sections in eq(2.15) have also to take the finite transverse momenta into account. This is because the transverse momenta of the incoming partons can have any kinematically allowed value and therefore cannot be neglected. In CCFM, the parton emissions are strongly ordered in angle of the emissions. In figure 2.7 the kinematics is shown and the angular ordering condition is:

$$\xi_0 < \xi_1 < ... < \xi_n < \Xi \tag{2.24}$$

This angular ordering in the phase space of the parton emissions dominates the process according to the CCFM evolution equations. We define the *rescaled transverse momentum*:

$$q_i = x_{i-1}\sqrt{s\xi_i} = \frac{p_{ti}}{1-z_i} \tag{2.25}$$

where p_{ti} is the transverse momentum of the emission i and $x_i = z_i x_{i-1}$. Now the angular ordering can be re-written as:

$$q_n > z_n q_n,\ q_n > z_{n-1}q_{n-1},\ ...\ ,\ q_1 > q_0 \tag{2.26}$$

Note that if x is very small then q_i can be any value in eq(2.26), i.e. p_t is not ordered, recovering the BFKL approximation, whereas if x is not very small eq(2.26) sets q_i ordering and therefore p_{ti} ordering, again the DGLAP approximation.

2.4 Multiple Interactions, MI.

We present here briefly the theoretical model of the MI used in the MC generator PYTHIA, see [9, 10]. This MC generator can simulate hadron-hadron collisions as well as *ep* collisions. In hadron-hadron collisions, MI of

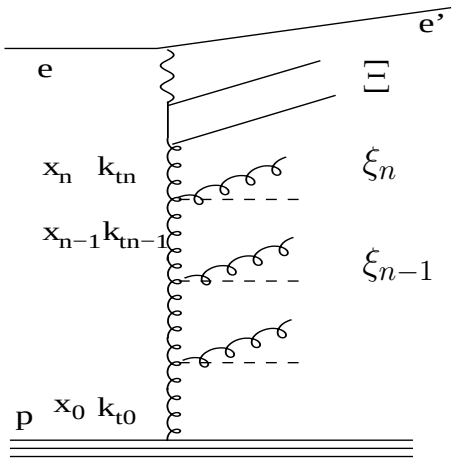

Figure 2.7: *CCFM parton evolution. The parton emission is ordered in angle of the emissions:* $\xi_0 < \xi_1 < ... < \xi_n < \Xi$.

the incoming partons of the hadrons can occur as an interaction of the hadron remnants due to the large parton densities. In *ep* collisions it happens in a similar way in the case of resolved photons. Figure 2.8 represents a multiple interaction event. Here, processes are characterized by one hard partonic scattering, with the highest virtuality of the process, and one or more other partonic scatterings with a lower virtuality, see figure 2.9 (note that PYTHIA uses DGLAP evolution). We show a list with the most important parameters that control MI in PYTHIA in table 2.1.

One of the free parameters of this model is $p_{\perp min}$, the relative transverse momentum between the two outgoing partons. For $p_{\perp min} \to 0$ the integrated interaction cross section, $\sigma_{int}(p_\perp > p_{\perp min})$, is larger than the total inelastic nondiffractive cross section, σ_{nd}, since the t-chanel gluon exchange dominates the $2 \to 2$ QCD cross section and this diverges like $\frac{dp_\perp^2}{p_\perp^4}$. This can be explained with the fact that if we have two interactions in one event this is counted twice in σ_{int} and only once in σ_{nd}. This counting procedure in σ_{int} leads to the identification:

$$\langle n \rangle_{p_{\perp min}} = \frac{\sigma_{int}(p_{\perp min})}{\sigma_{nd}} \tag{2.27}$$

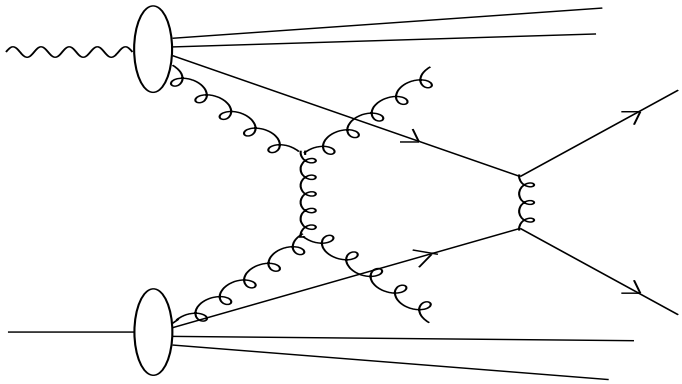

Figure 2.8: *Multiple interaction event. Partons from the photon and the proton interact more than once.*

where $\langle n \rangle_{p_{\perp min}}$ is the average number of interactions per event. Since $p_{\perp min}$ cannot be calculated from the theory, this parameter is tuned to data. At HERA this value is set to 1.90 GeV, see [2, 11–13]. There are two basic ways to apply this cut. The first one is to apply a step function $\theta(p_\perp - p_{\perp min})$ where the cross section would be zero below $p_{\perp min}$. A second one is to apply the factor:

$$\frac{\alpha_s^2(p_{\perp min}^2 + p_\perp^2)}{\alpha_s^2(p_\perp^2)} \frac{p_\perp^4}{(p_{\perp min}^2 + p_\perp^2)^2} \tag{2.28}$$

These partons from the hadron, figure 2.9, enter in hard interactions in decreasingly $p_\perp$ scale, $p_{\perp 1}$, $p_{\perp 2}$, $p_{\perp 3}$ and $p_{\perp 4}$. Althought there is no physical meaning in this ordering we do it for convinience, partly because the hardest interation will be the most important one in experimental measurements. Every hard interaction has associated its own parton evolution, initial state PS, from a starting $p_{\perp min}$. Here we have initial state PS and MI mixed up since a branching in the first hard interaction at $p'_{\perp 1}$, $p'_{\perp 1} > p_{\perp 2}$, reduces the available phase space for the second hard interaction. The other way around, the other possible process with $p_{\perp 2} > p'_{\perp 1}$ would represent a phase space reduction for the branching at $p'_{\perp 1}$. Therefore, it is useful to consider the initial state PS and MI in parallel using an unique decreasing sequence of $p_\perp$ for both processes. In this sequence, MI and initial state PS start a *phase space competition* that we will discus at the end of the section.

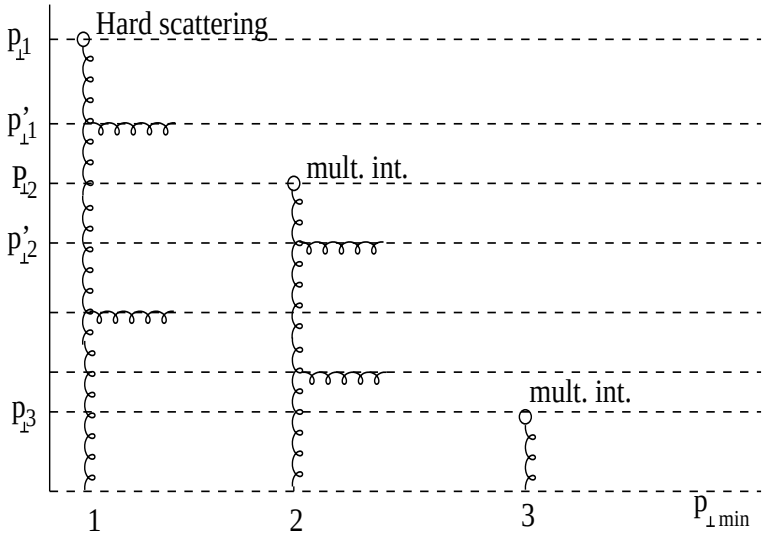

Figure 2.9: *Multiple interaction event. Partons from the photon and the proton interact more than once.*

The theory makes the hypothesis that the hard interactions take place independently of each other, leading to a Poisson distribution: $\mathcal{P}_n = \frac{\langle n \rangle}{n!} e^{-\langle n \rangle}$. This hypothesis is supported by the picture of the proton as a pancake, due to Lorenz contraction.

The interactions are ordered in $p_{\perp i}$: $\sqrt{s}/2 > p_{\perp 1} > p_{\perp 2} > ... > p_{\perp n} > p_{\perp min}$, according to the probability distribution:

$$\frac{d\mathcal{P}}{dp_\perp} = \frac{1}{\sigma_{nd}} \frac{d\sigma}{dp_\perp} exp\left(- \int_{p_{\perp i}}^{p_{\perp i-1}} \frac{1}{\sigma_{nd}} \frac{d\sigma}{dp'_\perp} dp'_\perp \right) \tag{2.29}$$

where the exponential expression, similar to eq(2.23), is a factor and gives the probability to have no MI between $p_{\perp i}$ and $p_{\perp i-1}$.

We can also include in the model a dependence on the impact parameter b, see figure 2.10. A small impact paremeter means central collision, whereas a large one means a peripheral collision. At small values of b, central collisions, the overlap of the proton and the resolved hadron-like structure of the photon is very large, and therefore it gives also a larger MI probability. If we denote the matter overlap with $\Psi(b)$, we can generalize eq(2.29) as follows:

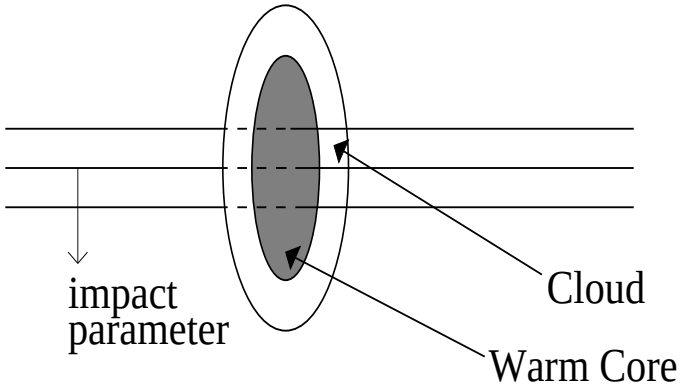

Figure 2.10: *Representation of a hadron with a double Gaussian distribution.*

$$\frac{d^3\mathcal{P}}{dp_\perp d^2b} = \frac{\Psi(b)}{\langle\Psi\rangle}\frac{1}{\sigma_{nd}}\frac{d\sigma}{dp_\perp} exp\left(-\frac{\Psi(b)}{\langle\Psi\rangle}\int_{p_{\perp i}}^{p_{\perp i-1}}\frac{1}{\sigma_{nd}}\frac{d\sigma}{dp_\perp^{'}}dp_\perp^{'}\right) \tag{2.30}$$

This overlap function, Ψ, is parametrized in PYTHIA by a Gaussian distribution, which represents a hadronic core, or by a double Gaussian, where one could imagine it as hard hadronic core surrounded by a pion cloud, see figure 2.10.

Since no multiple parton densities are available, a simple ansatz is taken into account for the different phase space available in MI:

- For an interaction i, with momentum fraction x_i, we rescale the parton distributions: $f(x) \rightarrow f(x/X)/X$, where X is the remaining momentum fraction after n interactions, $X = 1 - \sum_{i=1}^{n} x_i$.

- The valence distribution of flavour f after n interactions, q_{fvn}, is normalized to the number of valence quarks with flavour f, N_{fvn}, scaling the original distribution by N_{qvn}/N_{fv0}

- In the case that in the hard interaction a sea quark is picked up, q_s, we assume this comes from $g \rightarrow q_s + q_{\bar{s}}$, where $q_{\bar{s}}$ is the antisea quark of q_s. If the gluon has a momentum fraction y, the $q_{\bar{s}}$ carries a fraction x, $x = y - x_s$. The $q_{\bar{s}}$ distribution is given by:

$$q_{\bar{s}}(x; x_s) \propto \int_0^1 g(y) P_{g \to q_s q_{\bar{s}}}(z) \delta(x_s - zy)\, dz \tag{2.31}$$

where we neglected other interactions and other perturbative evolutions of $q_{\bar{s}}$ and $P_{g \to q_s q_{\bar{s}}}$ is the DGLAP *splitting kernel*.

In summary of the different possibilities for PYTHIA, we have a procedure for the MI hard scatterings and the initial state PS, which are calculated together since they have to "*compete*" for the available phase space. In addition, two different kinds of cuts for $p_{\perp min}$ can be chosen, an abrupt one given by a step function and a continuous one given by the factor in eq(2.28). The impact parameter dependence can be introduced and simple or double Gaussian distributions can be selected to model the hadron content distribution in the proton. All these options are controlled basically by the parameters MSTP 82 and PARP 81-83, which are summarized in table 2.1.

2.5 Monte Carlo event generators.

In the previous sections we have given a theoretical overview. The theoretical predictions are usually implemented in Monte Carlo event generators. The event generation can be factorized in several processes: initial state parton shower, hard scattering, final state parton shower and hadronization (see figure 2.11).

In this thesis we use the DGLAP based Monte Carlo generators RAPGAP and PYTHIA. A Monte Carlo generator based in CCFM is CASCADE [14]. In the following we describe briefly the event generation steps.

- Initial and Final State Parton Shower.

  Higher order QCD radiation can be approximated by PS, i.e. quarks and gluons radiated by the incoming and/or outcoming partons of the hard scattering, are called initial state and final state PS. In section 2.3 we presented the DGLAP, BFKL and CCFM parton evolutions for these in- and outcoming partons. Equation 2.23 steers this process for generators using DGLAP where no multiple interactions are included, whereas in the multiple interaction model the different incoming partons in the different hard scatterings have a competition for the phase space available, as explained at the end of section 2.4.

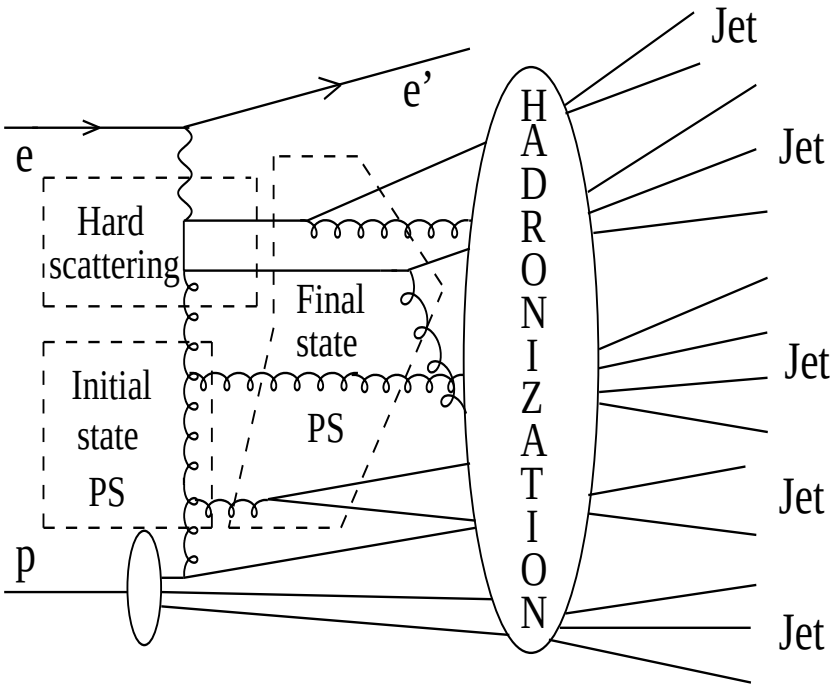

Figure 2.11: *Schematic picture of an electron-proton collision. The different subprocesses: hard interaction, initial and final state radiation and hadronization are shown.*

- Hard Scattering.

  The hard scattering is calculated using QCD Matrix Elements, ME. The event generators used here calculate the ME only in Leading Order, LO, in α_s.

- Hadronization.

  The hadronization is the process where the quarks and gluons, coloured particles, go into observable particles, i.e. mesons and hadrons. This is a non-perturvative process and cannot be calculated but modelled. An important feature of the hadronization is that there is no heavy quark production in the fragmentation process. Two models are the independent and the Lund String fragmentation models and are described in [2]. In the independent fragmentation the partons pick up quarks from the $q\bar{q}$ pairs from the vacuum when forming mesons. This model does not take into account any color consideration. The Lund String model considers the strong interaction force between partons (these are coloured particles with a relative momentum) with a string-like force. The kinetic energy from the coloured particles is transferred to the string. This energy is used to create $q\bar{q}$ pairs when the string

has energy enough to break and produce them. The created pairs are also bounded by a new string. When the energy in the strings is not enough to create new mesons and hadrons the process stops.

MSTP 82	Short description	Abbreviation
1	same probability for all events and abrupt $p_{\perp min}$ cut.	MI-1
2	same probability for all events and continuous $p_{\perp min}$ cut.	MI-2
3	impact parameter and Gaussian matter distribution with continuous $p_{\perp min}$ cut.	MI-3
4	impact parameter and double Gaussian matter distribution with continuous $p_{\perp min}$ cut.	MI-4

Parameter: PARP	Short description
81	effective $p_{\perp min}$ for MI-1
82	regularization scale of the transverse momentum spectrum for $MSTP\ 82^2 \geq 2$, at the reference energy scale PARP 89 with the degree of energy rescaling given by PARP 90
83	In double Gaussian: fraction of the total hadronic matter within a core of radius PARP 84
84	Core radius in double Gaussian matter distribution.
85	Probability that the MI produces two gluons with color connections to the 'nearest neighbors'
89	Reference energy scale
90	Power of the energy-rescaling term of $p_{\perp min}$

Table 2.1: *Summary of the parameters relevant for MI in* PYTHIA.

[2]For these options it is: $p_{\perp min} = (PARP82)\left(\frac{s}{PARP89}\right)^{PARP90}$

Chapter 3

Jets and Heavy Quark Identification

In this chapter we study how the calculations at the parton level, i.e. the outgoing quarks from the hard scattering including also multiple interactions, and the gluons from the initial and final state parton shower, are related to the hadron level. This relation is interesting since the hadrons are the particles we can measure.

For this purpose we introduce the concept of jet and its properties. We examine also two jet finder definitions: the K_t *algorithm*, a cluster-type algorithm, and the $CDF-CONE$ *algorithm*, a cone-type one. The results of these jet finder will be compared in the next chapters.

Since the main purpose of this thesis is the study of the heavy quark production, we are interested in the heavy quark identification, the charm quark, at the hadron level with the help of the jets. We discuss three possible heavy quark identification methods with the jets. In the next chapters these methods will be used to calculate differential cross sections and to compare their results.

3.1 Charm Jet Concept.

The outgoing partons from the hard scattering and the initial and final state PS studied in chapter 2 are coloured particles. The colour charge confinement

prevents the measurement of any parton before hadronization. This means we can only measure the hadrons (figure 2.11).

A jet is defined as a collimated stream of particles and energy. After initial state PS, hard scattering and final state PS, all partons hadronize. The particles produced from high energetic partons are expected to follow more or less the direction of the parton, thus producing a jet of particles. There are different methods for the combination of particles into jets, i.e. there is no unique definition for jets. In general, a jet algorithm should fulfil the following properties:

- it has to be easy to implement: both in the experimental analysis and in the theoretical calculations.

- it should provide and define finite cross sections at any order of perturbation theory. It is therefore necessary that the definition is infrared safe, i.e. insensitive to emission of low energy particles, and collinear safe, i.e. insensitive when replacing two collinear particles by a single one with the summed momentum.

- the sensitivity of the jet algorithm to the details of the hadronization should be small.

The jet algorithms take the objects under study, called *seeds*, which can be partons, hadrons, calorimeter cells, tracks, etc, and combine them with a certain algorithm to construct the jets. This procedure together with the stopping conditions define the jet algorithm.

3.1.1 K_t Algorithm.

There are two modes [15]: the inclusive and the exclusive one.

- Inclusive mode.

  The algorithm works with the final state objects, i, and the beam, B, and from them it defines the *resolution variables*: d_{iB}, between the final state objects and the beam, and d_{ij}, between two final state objects i and j. The definition of these *resolution variables* is left to a particular algorithm but are defined such that, at small angles, they are the squared relative transverse momentum of i with respect to the beam, B, and to the object j respectively. The procedure is:

- Calculate the *resolution variables* for the final state objects and the beam.

- Find the smallest value among all the d_{iB} and d_{ij}, d_{min}. Now there are two possibilities. First: if d_{min} is one of the d_{ij} values, then the two final state objects i and j are combined into a single one. Second: if d_{min} is one of the d_{iB}, then the object i is defined as a jet, i.e. not considered as an object any more.

- The *resolution variables* are recalculated with the objects that are left and the procedure starts again unless there are no more objects to be taken into account.

The combination scheme of two objects i j is also left to a particular algorithm. An example of *resolution variables* is:

$$d_{iB} = E_i^2\theta_{iB}^2 \simeq k_{\perp iB}^2 \; for: \; \theta_{iB} \to 0 \tag{3.1}$$

$$d_{ij} = min(E_i^2, E_j^2)\theta_{ij}^2 \simeq k_{\perp ij}^2 \; for: \; \theta_{ij} \to 0 \tag{3.2}$$

An example of combination scheme is to add the 4-vectors producing "massive" jets:

$$p_{ij} = p_i + p_j \tag{3.3}$$

- Exclusive mode.

  In this mode we define also a stopping parameter d_{cut}, which has dimensions of energy squared. The procedure is:

  - Calculate the *resolution variables* as in the previous mode.

  - Find d_{min} as in the previous mode. Now we have three possibilities. First: if $d_{min} > d_{cut}$ then all the objets at this stage are defined as jets. Second: if a d_{ij} is the smallest value then the objects i and j are combined into a single one. Third: if a d_{iB} is the smallest value then the object i is included in the *beam Jet*.

  - The procedure is repeated until all the objects are defined as jets.

  It is important here to stress that the definition of d_{cut} separates the hard final state from the soft beam remnants, since it stops the procedure when all the objects fulfil the cut: $d_{min} > d_{cut}$, which imposes a hard scale for the process.

In the following we only refer to the K_t *algorithm* in the inclusive mode.

An important feature of the Inclusive mode is that at the end of the procedure all the particles end up in jets, whereas in the Exclusive mode some of the particles are included in the *beam Jet*.

3.1.2 CDF-CONE Algorithm.

The basic idea is the hypothesis that a jet can be defined from those particles in a cone around the direction of the parton. This cone is defined in the $\eta - \phi$ space, where η is the pseudo-rapidity defined in eq 2.4, and ϕ is the azimuth angle.

The algorithm [16] starts creating a list of particles with E_t above a threshold, E_0, and these particles are used as *seeds* for the process:

- The transverse momenta of all the particles within a cone of radius R_0 around each *seed* particle are added. This radius is defined as:

$$R = \sqrt{\Delta\eta^2 + \Delta\phi^2} = \sqrt{(\eta_i - \eta_0)^2 + (\phi_i - \phi_0)^2} \tag{3.4}$$

where η_0 and ϕ_0 are the center of the cone coordinates, the *seed*, and η_i and ϕ_i the particle coordinates, satisfying the condition: $R < R_0$.

- Now, the centre of gravity of each cone is calculated. If the particles within the cone of radius R_0 around the centre of gravity are the same as the particles in the cone centered in the seed, this is defined as a jet and the seed is removed from the list of seeds. If not, the centre of gravity is taken as a new *seed* and we iterate again.

The iteration stops when there are no *seeds* left.

Both the K_t and the $CDF-CONE$ algorithms are not free of problems. For example, the cone algorithm definition is not infrared safe in events with final states with more than three partons. Information about it can be found in [17–20]. The K_t algorithm, although infrared and collinear safe, has the problem that the CPU time used increases very fast with the particle multiplicity, which can be a problem at colliders like the Large Hadron Collider (LHC) at CERN, see [21].

3.2 Charm Jet Selection.

In this section we study three methods to identify the charm content of the jets.

All the methods described below have in common the tagging of charm via a D^* particle, which arises from the charm fragmentation. In the MC study presented here, the D^*, independently of the decay chanel, is required to satisfy: $P_t > 2\ GeV$, $\mid \eta \mid < 1.5$. If an event contains more than one D^* the study is repeated for each of them independently.

Leading Particle Method.

In this method we use one of the jet algorithms to find the jets. Among the decay particles of the D^* the one with the largest transverse momentum in the laboratory frame is taken as the Leading Particle, LPD. The jet which contains the LPD is identified as the $D^*\ Jet$.

Although at high P_t all the decay particles of the D^* are supposed, in principle, to be in the same jet, it was found that most of the D^* decay products end up in several jets. Therefore we defined a LPD in order to be able to define the D^*Jet according to the idea of jet.

D^* Meson as Stable Particle Method.

The D^* decay particles are replaced by the D^*. This is done to include the D^* unconditionally in one of the jets when executing the jet algorithm, and to exclude the possibility that the decay particles go into different jets. The jet containing the D^* is called the D^*Jet.

This method is based on the idea that the purpose of the jet algorithms is to find the correlation between the partons, in this case the charmed quark represented by the D^* particle, and the hadron level. Experimentally this can be also done with the reconstructed D^*.

Cone Method.

This method follows the same principle as the $CDF-CONE\ algorithm$ described in the previous section. In a similar fashion, a distance R is defined in analogy to the cone radius, R of eq(3.4). The distance is now taken from the D^* particle to the jets. The jet with smallest distance, R_{min}, to the D^* particle is defined as the D^*Jet, when the condition $R_{min} < 1$ is fulfilled.

Chapter 4

Short introduction to the H1 Detector at HERA

This chapter introduces the H1 detector at the HERA (Hadron-Elektron-Ring-Anlage) particle accelerator. Although this thesis does not contain any data analysis, except for the data taken from the Thesis of Gero Flucke [3], we need to take into account how we measure. Since we present an study on multiple interaction in heavy quark production, which will be contrasted to data, we need to understand the detector to apply the necessary cuts in the study.

After a general presentation of HERA we give a short description of the CDF (Central Tracking Detector), the calorimeters and the luminosity system.

4.1 The Particle Accelerator HERA.

The particle accelerator HERA (name taken from one of the twelve olympians of the greek mythology and Zeus wife) at the DESY (Deutsches Elektronen-SYnchroton) laboratory is situated in Hamburg, Germany, and has a circunference of 6.3 Km. Electrons (or positrons), with an energy of 27.6 GeV, and protons with an energy of 920 GeV (820 GeV before 1998) are accelerated in bunches and collided at four interaction points, two of them are the H1 and ZEUS experiments ($\sqrt{s} \approx 320\ GeV$). The particles are accelerated in DESY

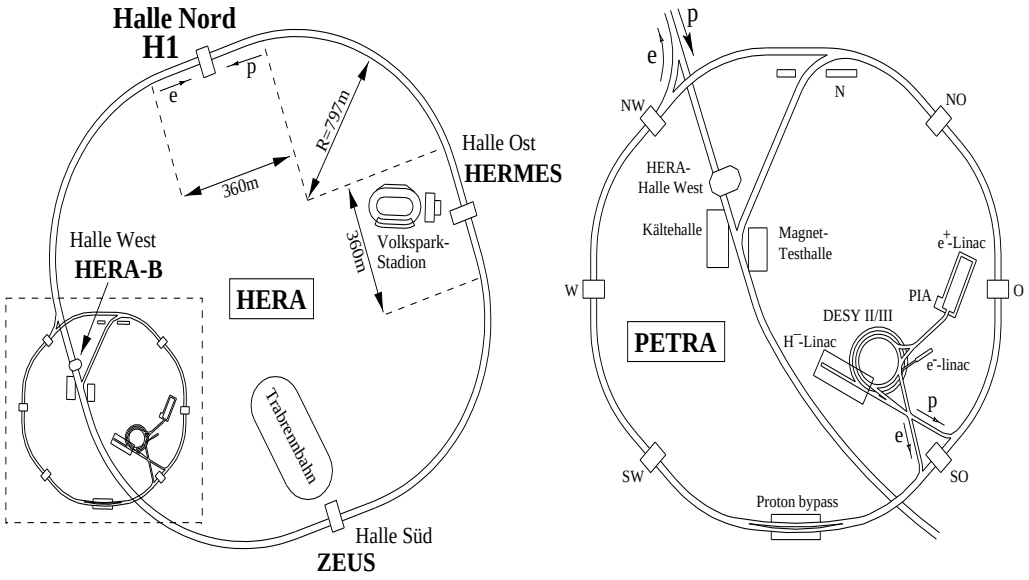

Figure 4.1: *On the right side the DESY and PETRA facilities, and on the left the HERA ring and the halls: H1, ZEUS, HERMES and HERA-B.*

and PETRA rings and then injected into the HERA ring, with an energy of 12 GeV and 40 GeV for electrons and protons respectively, see figure 4.1.

4.2 The H1 Detector.

The H1 detectector consists on multiple subdetectors and components, which due to the higher energy coming from the proton side is asymetrically constructed, i.e. most of the created particles go to the forward region (proton direction) and therefore a better resolution is needed there. The H1 detector is described in detail in [22, 23]. The most important parts for this thesis are the Central Tracking Detector (CTD), the calorimeters and the luminosity system.

4.2.1 Central Tracking Detector.

The task of the tracking is to reconstruct and identify charged particles and to measure their momenta. The central tracking detector covers the polar region: $20^0 < \theta < 160^0$.

From the beam pipe to the outer part of the detector, the CTD consists on the Central Silicon Tracker (CST), the Central Inner Proportional Chamber (CIP), the Central Inner z-drift Chamber (CIZ), the Central Jet

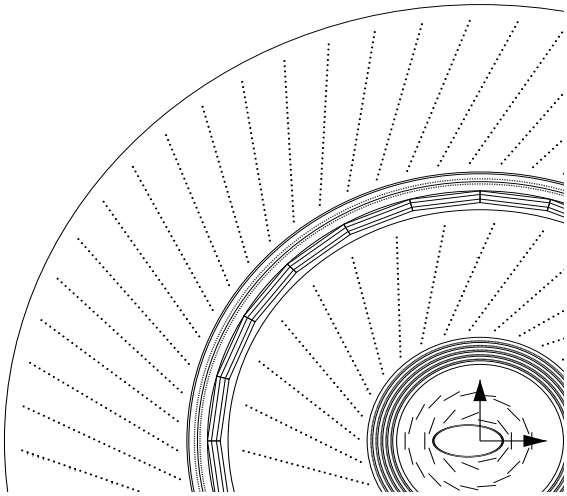

Figure 4.2: *Transverse section of the Central Tracking Detector.*

Chamber 1 (CJC1), the Central Outer z-drift Chamber (COZ), the Central Outer Proportional Chamber (COP) and the Central Jet Chamber 2 (CJC2).

With a magnetic field of about 1.5 T in the tracking detector, the charged particles trajectories are bend and in this way the particle momenta can be calculated. The main tracking detector, the CJC, are two coaxial cylinders filled with gas, which is ionized by charged particles when crossing the detector. The electrons from the ionization drift to the wires in a strong electric field, and one can measure the position of the charged particle.

4.2.2 Calorimeters.

The main task of the calorimeters is to measure the energy of charged and neutral particles. The two main calorimeters are the Liquid Argon (LAr) calorimeter and the spaghetti calorimeter (SpaCal).

The LAr is a stack of lead, for detection of the electromagnetic part of the incident particles, and steel plates, to detect the incoming hadrons. Both parts are surrounded by liquid argon. The electromagnetic component is in the inner part, whereas the hadronic component is in the outer part of the calorimeter. It covers the polar region: $4^0 < \theta < 154^0$. When hadrons, electrons and photons are absorved, particle showers are produced through bremsstrahlung and pair production, so that the energy of the particles is deposited in the calorimeter. When these showers enter in the liquid argon, they ionize it and the deposited energy can be measured.

The SpaCal has also an electromagnetic part and a hadronic part and covers the polar region: $153^0 < \theta < 177.5^0$, i.e. $1 < Q^2 < 100\ GeV^2$, which is out of our region of interest.

4.2.3 Luminosity System.

For the luminosity measurement we use the Bethe-Heitler process $ep \rightarrow ep\gamma$. Since the cross section is very well known, the detection of this process allows us to calculate the luminosity. The luminosity is monitored by two Čerenkov calorimeters, which detect this process. They are the electron tagger ET33, at z=-33.4m, and the photon detector (PD), at z=-101.8m both elements in the electron direction. The electron tagger is also used to tag photoproduction and the photon detector is also used to detect hard photons from the initial state QED radiation in deep inelastic scattering.

Chapter 5

Photoproduction of D^* using RAPGAP as event generator

The aim in this chapter is to understand processes which consist of one jet containing a charm quark from the hard interaction. The direct and resolved processes are studied, as well as the parton showering mechanism. The charm is tagged by the D^* particle and the D^*Jet. The other jet, which we will denote simply as jet, does not contain the tagged charm but is also reconstructed to further constrain the hard subprocess. If an event contains more than one D^* particle we consider it as if it were two different events, one per each D^* particle. Cross sections were calculated for D^* photoproduction, with $Q^2 < 0.01\ GeV^2$, in the kinematic region of $171 < W < 256\ GeV$ and $0.29 < y < 0.65$.

As a tool to get an easy access to the Monte Carlo, MC, event generator information we use the hztool package [24]. First we use the $K_t\ algorithm$ to find jets and then we compare the results with the $CDF-CONE\ algorithm$, applied in the laboratory frame. The D^* particle is required to satisfy: $P_t > 2\ GeV$ and $\mid \eta \mid < 1.5$, which corresponds to the central H1 detector region. These cuts will be very important when comparing our results with real data because they ensure a proper D^* detection and tracking. It was found that mostly the D^* decay products go into several jets. For such cases and in order to define the D^*Jet, we search for the leading particle of the decay, see section 3.2, by tracing back the decay products of the D^* independently of the decay chanel. This can be easily done with MC event generators, but

W	$171 < W < 256\ GeV$
y	$0.29 < y < 0.65$
Q^2	$Q^2 < 0.01\ GeV^2$
η_{D^*}	$\mid \eta_{D^*} \mid < 1.5$
$P_t^{D^*}$	$P_t^{D^*} > 2\ GeV$
η_{Jet}	$-1.5 < \eta_{Jet} < 2.7$
P_t^{Jet}	$P_t^{Jet} > 3\ GeV$

Table 5.1: *In this table the cuts for W, y and Q^2 are defined as well as for D^* particles and jets (also the D^*Jet).*

is also possible experimentally after the D^* has been reconstructed. For the other jet we apply the following cuts: $P_t > 3\ GeV$ and $-1.5 < \eta < 2.7$, where we can go to a more "forward" region because experimentally for jets one can use also the information from the forward calorimeters, whereas for the D^*Jet the tracking is needed. Table 5.1 contains a summary of the cuts.

We use RAPGAP 3.1 [1] using different sets of parameters, see Table 5.2, to investigate different subprocesses, such as electron-gluon interactions or resolved photon processes (section 5.1) and contributions from different types of parton showers, PS, (section 5.2).

We also study the K_t and $CDF-CONE\ algorithms$, described in chapter 3, at the Monte Carlo event generator level (section 5.3).

5.1 Direct and Resolved Photon Cross Sections

In this section the angular distribution of D^* and jet in direct and resolved photon processes is investigated. The jets are reconstructed with the $K_t\ algorithm$.

In Figure 5.1a) the differential cross sections as a function of η of the jet and the D^* for resolved photon processes are presented. Here, the D^* appears

Parameter	Resolved photon	Direct process
IPRO	18	14
PTCU	2	5
NFQC	4	3
IHFL	4	3

	No PS	Initial	Final	Initial and Final
IFPS	0	1	2	3

Table 5.2: *In this table are shown the parameters for resolved photon processes and for direct ones as well as for no PS, initial, final, initial and final state PS.*

clearly more often in the negative region of η whereas the jet appears more in the positive region. In Figure 5.1b) the differential cross sections $d\sigma/\eta_{Jet}$ and $d\sigma/\eta_{D^*}$ are compared for direct processes. Here we see that D^* appears more often in the negative η region as compared to the jet. This is suggested from the diagrams involved, see figure 2.4, where it becomes clear that in resolved photon processes the jets are produced more often in the proton direction.

In Figure 5.1b), where direct processes are shown, both the jets and the D^* have the largest cross sections in the negative η region. This results in $\Delta\eta$ centered around zero. In Figure 5.1a), where resolved photon processes are plotted, the distributions for the jets and the D^* are different, resulting in a $\Delta\eta$ at negative values.

In figure 5.2 we present the cross sections of the process $e + D^* \rightarrow e' + D^* + Jet + X$ as a function of $\Delta\eta$, which is defined as the difference between η_{LPDJet} and η_{Jet}. The contributions, in the phase space defined in Table 5.1, of the direct processes and resolved photon processes are shown separately. The average value for $\Delta\eta$ in direct processes is $\Delta\eta \simeq -0.7$, whereas for the resolved photon events it is $\Delta\eta \simeq -1.1$. The reason can be explained with the different η distributions, for D^* and jet in direct and resolved photon events.

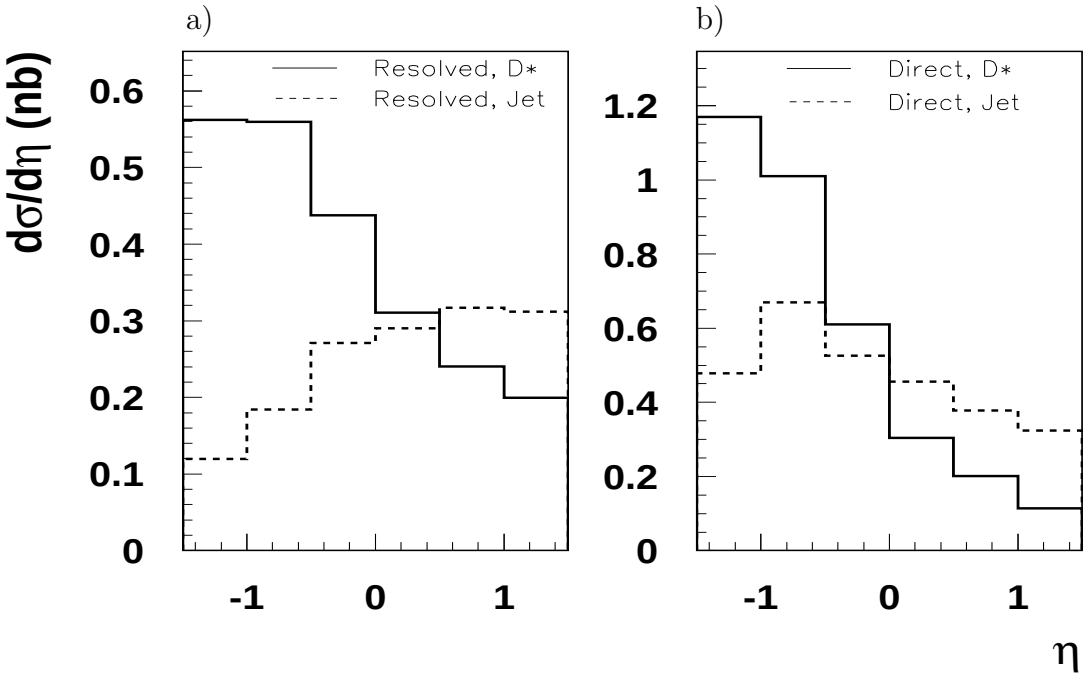

Figure 5.1: *Differential cross sections $d\sigma/d\eta_{D^*}$ and $d\sigma/d\eta_{Jet}$ for resolved processes (a) and for direct $\gamma+g \rightarrow c\overline{c}$ events (b). The more negative mean value of $d\sigma/d\Delta\eta_{LPDJet-Jet}$ in resolved events comes from the negative η region.*

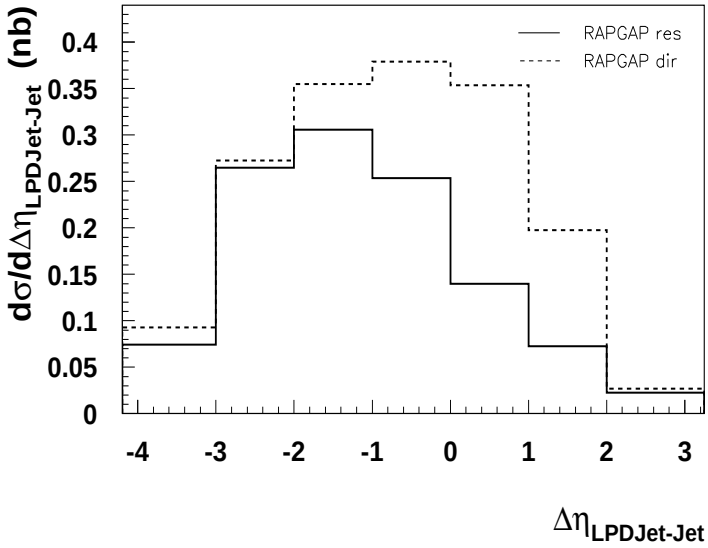

Figure 5.2: *Differential cross section $d\sigma/d\Delta\eta_{LPDJet-Jet}$. The resolved photon events (solid line) are shifted to the left in comparison to the direct $\gamma+g \rightarrow c\overline{c}$ (dashed line).*

5.2 Cross Sections with different Parton Shower settings.

With the MC generator RAPGAP the different contributions of initial and/or final PS can be studied separately. In Figure 5.3 and 5.4 the cross sections $d\sigma/d\Delta\eta_{LPDJet-Jet}$, $d\sigma/dP_t^{D^*}$ and $d\sigma/d\eta_{D^*}$ are shown for direct processes with and without initial and final state PS.

In figure 5.3 $d\sigma/d\Delta\eta_{LPDJet-Jet}$ is shown for cases without and with initial and/or final PS. Here one can observe that the initial state PS contributes to the negative $\Delta\eta_{LPDJet-Jet}$ region, whereas final state PS contributes to positive region. It is interesting to observe that the cross section becomes smaller if both initial and final state PS are included.

To understand this observation in more detail, we show in figure 5.4 the differential cross sections as a function of P_t and η of the D^* without any cut. In the region $2 < P_t^{D^*} < 12\ GeV$ the larger cross section is for initial PS whereas in the whole region, $0 < P_t^{D^*} < 12\ GeV$, all the cross sections are, by construction, equal within errors. The difference therefore comes from the region $0 < P_t^{D^*} < 2\ GeV$, see figure 5.5, where the larger cross sections are, in decreasing order, for final PS, no PS, initial and final PS and initial PS events. Therefore the cut in $P_t^{D^*}$ is responsible for the different cross sections in figure 5.3 for different PS settings in $d\sigma/d\Delta\eta_{LPDJet-Jet}$, because, in general, the initial state PS increases $P_t^{D^*}$, whereas final state PS decreases it.

5.3 Jet finder dependence.

In this section we use the $CDF - CONE\ algorithm$ to perform the same analysis as in the previous section. Since the definition of a jet is not unique, the idea is to check the dependence of the previous results on the choice of the jet algoritchm.

We saw that one of the parameters to be chosen is the radius, R. In figure 5.6 cross sections using different radii are shown for direct events with initial and final state PS. We also include the $K_t\ algorithm$ cross sections for comparison. Figure 5.6a) shows the differential cross section $d\sigma/dP_t^{D^*}$ and figure 5.6b) $d\sigma/d\eta_{D^*}$. In both cases the best agreement between the K_t and

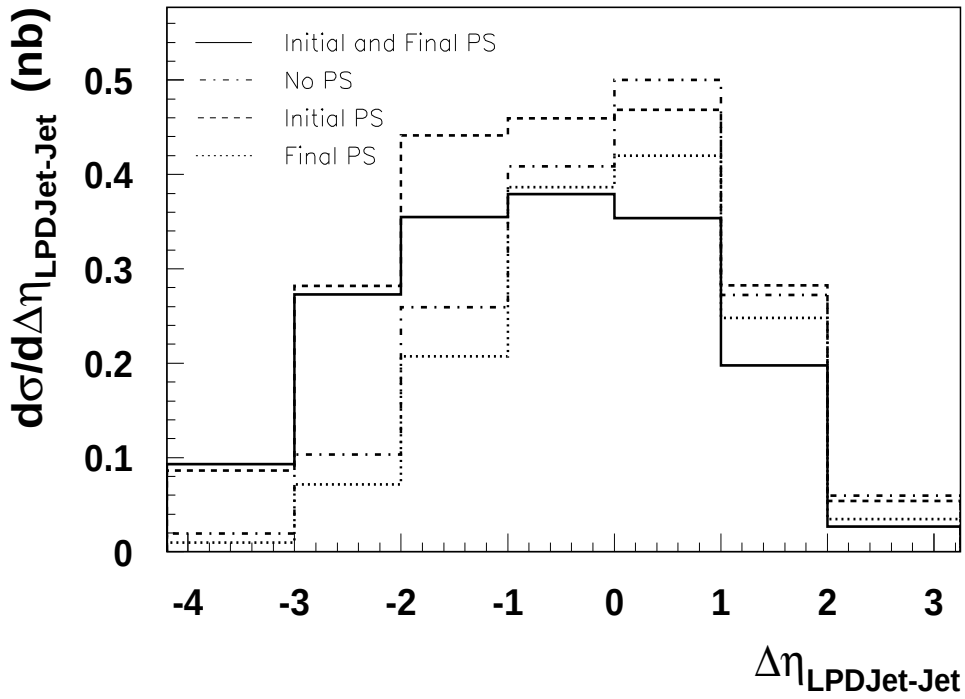

Figure 5.3: *Cross sections $d\sigma/d\Delta\eta_{LPDJet-Jet}$ for direct processes and different PS settings, using the K_t algorithm. The differences in the cross sections are explained by the cut $P_t^{D^*}$ (see figure 5.4 for explanation).*

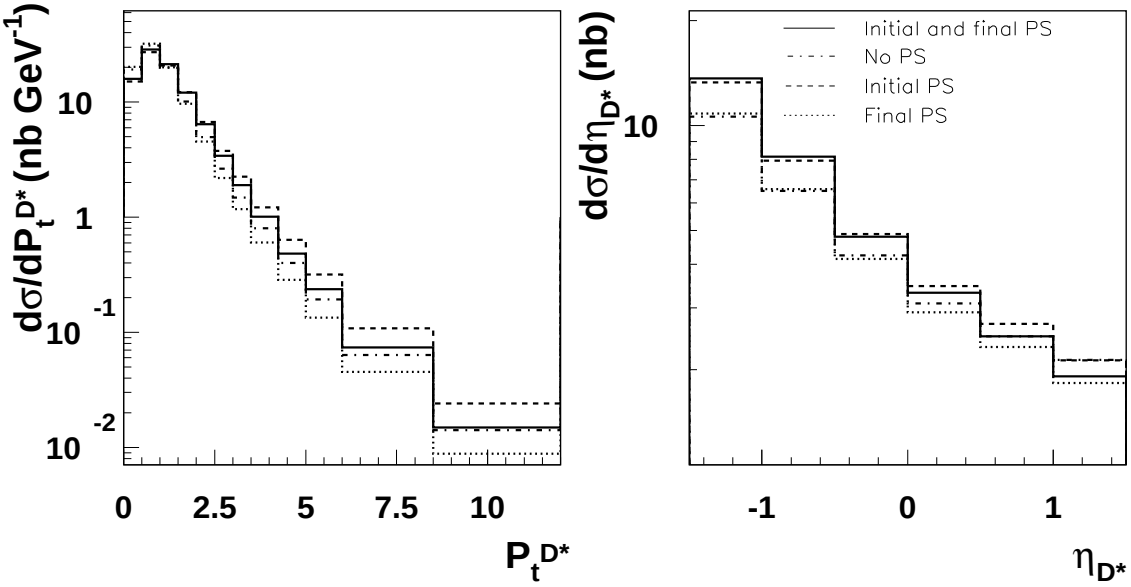

Figure 5.4: *Cross sections $d\sigma/dP_t^{D^*}$ and $d\sigma/d\eta_{D^*}$ for direct processes and different PS settings. The region $0 < P_t^{D^*} < 2$ GeV explains the differences in the cross sections shown in figure 5.3.*

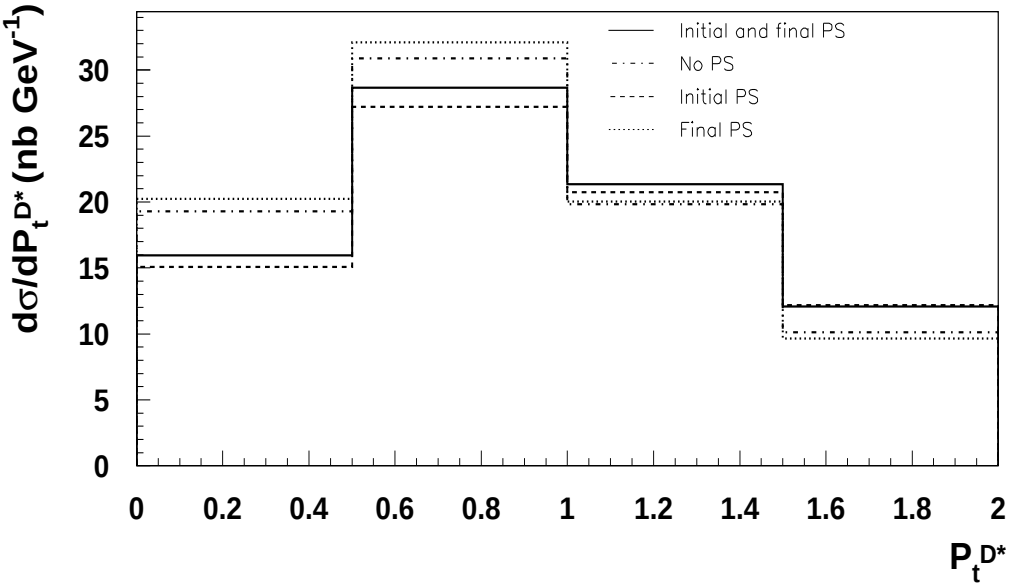

Figure 5.5: *Cross sections $d\sigma/dP_t^{D^*}$ for direct processes and different PS settings in the region $0 < P_t^{D^*} < 2$ GeV which explains the differences in the cross sections shown in figure 5.3.*

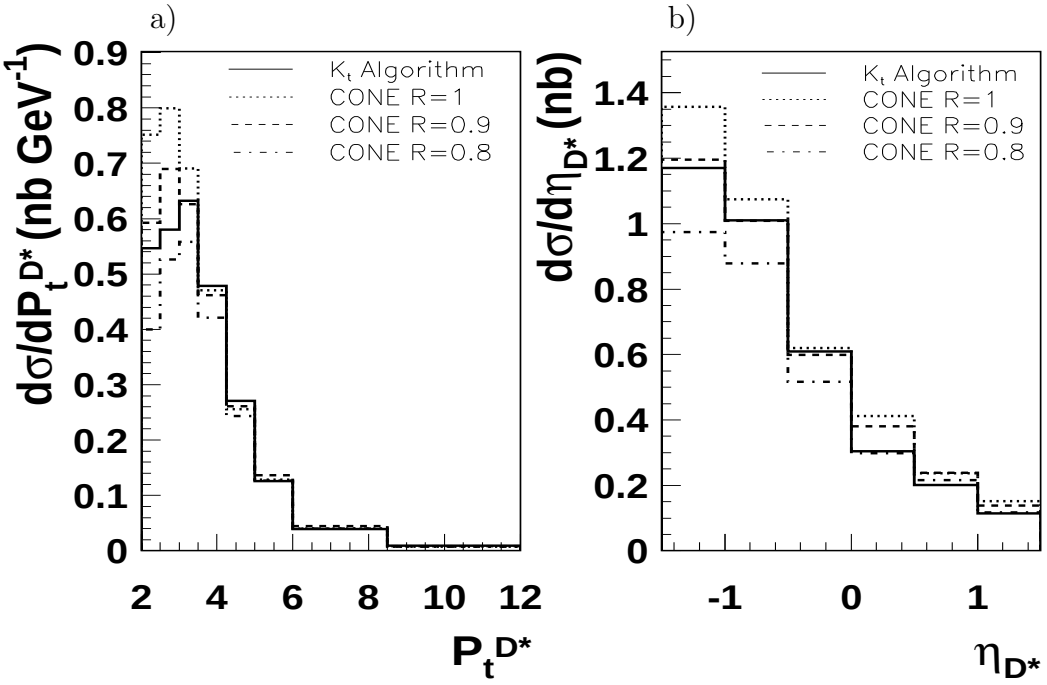

Figure 5.6: *Differential cross sections $d\sigma/dP_t^{D^*}$ and $d\sigma/d\eta_{D^*}$ for direct events with initial and final state PS. The best fit to the K_t algorithm corresponds to the cone algorithm with radius $R = 0.9$.*

the $CDF - CONE$ algorithms is observed for $R = 0.9$. The agreement is very good for $P_t^{D^*} > 3\ GeV$, whereas the other settings fit well only above $3.5\ GeV$. For the next comparisons in this section we will run therefore the $CDF-CONE\ algorithm$ with $R = 0.9$. The differences in the low P_t region arise because the transverse momenta of the decay particles can be large and the particles may not end up in one jet, see figure 5.7, whereas at large P_t the decay particles of the D^* are boosted towards the direction of the D^* and the jet algorithms yield the same results.

In Figure 5.8 we show the cross section $d\sigma/d\Delta\eta_{LPDJet-Jet}$ for resolved and direct events. As in Figure 5.2, the mean value in resolved photon events is shifted to smaller $\Delta\eta$ values. Figure 5.9, as in Figure 5.1, shows that this shifted value of $d\sigma/d\Delta\eta_{LPDJet-Jet}$ in resolved events comes from the negative η region. A direct comparison between the cross sections $d\sigma/d\Delta\eta_{LPDJet-Jet}$ calculated with the K_t and $CDF-CONE\ algorithms$ is shown in figure 5.10, where we find differences smaller than 15% except in the forward region where they can be about 25%.

In Figure 5.11 we present again the differential cross section $d\sigma/d\Delta\eta_{LPDJet-Jet}$

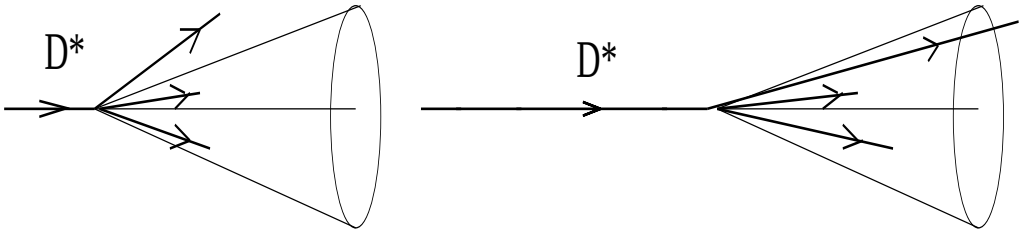

Figure 5.7: *For small $P_t^{D^*}$ (left) the D^* transverse momenta of the decay particles can become comparable to $P_t^{D^*}$. Then, the direction of the Leading Particle can be very different from the direction of the D^* particle and get different results. The cone is added to have a spatial reference in both cases.*

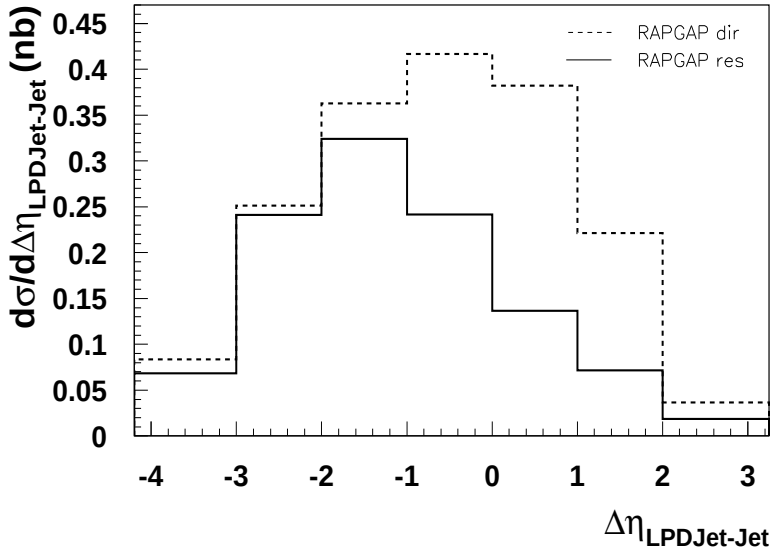

Figure 5.8: *Cross sections $d\sigma/d\Delta\eta_{LPDJet-Jet}$ for direct and resolved processes where the $CDF-CONEalgorithm$ was used. Althought there are some small differences between the cross sections presented here and the ones in figure 5.2, the conclusions are the same as before.*

for the $CDF-CONE$ *algorithm*, similar to Figure 5.3. Although there are some differences in the cross sections, the relations between the different PS settings remain and therefore also the conclusions of the previous section. This can also be seen in Figure 5.12, where the ratios between the $CDF-CONE$ and K_t *algorithm* for the $d\sigma/d\Delta\eta_{LPDJet-Jet}$ cross sections are presented. The differences are below 15%.

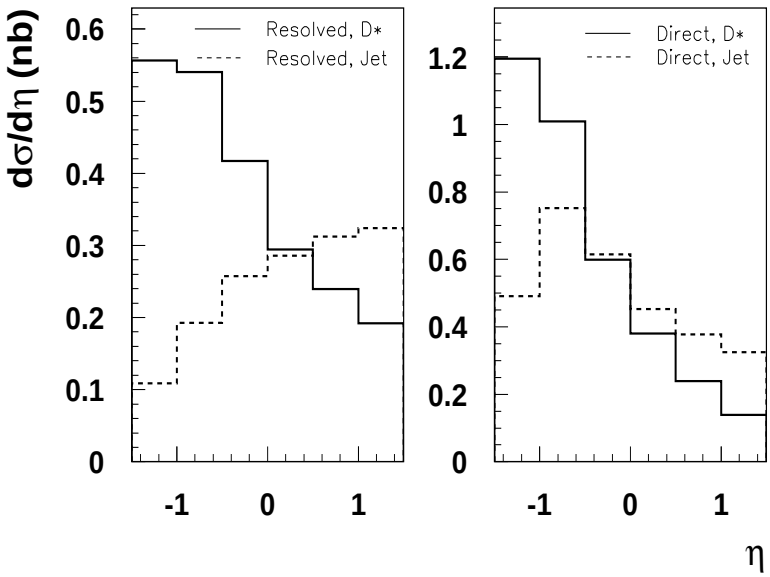

Figure 5.9: *Differential cross sections $d\sigma/d\eta_{D^*}$ and $d\sigma/d\eta_{Jet}$ for direct and resolved processes. The more negative mean value of $d\sigma/d\Delta\eta_{LPDJet-Jet}$ in resolved events comes from the negative η region.*

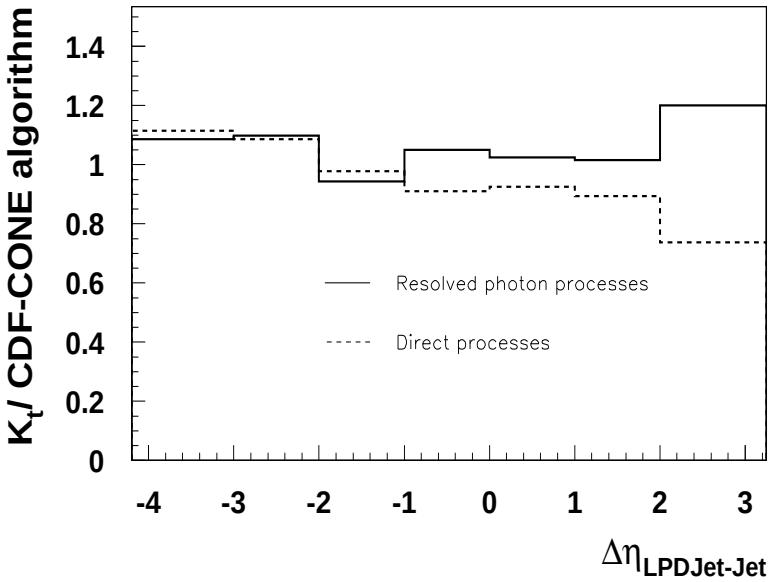

Figure 5.10: *Ratios between $CDF-CONE$ and K_t algorithm cross sections $d\sigma/d\Delta\eta_{LPDJet-Jet}$ for direct and resolved processes.*

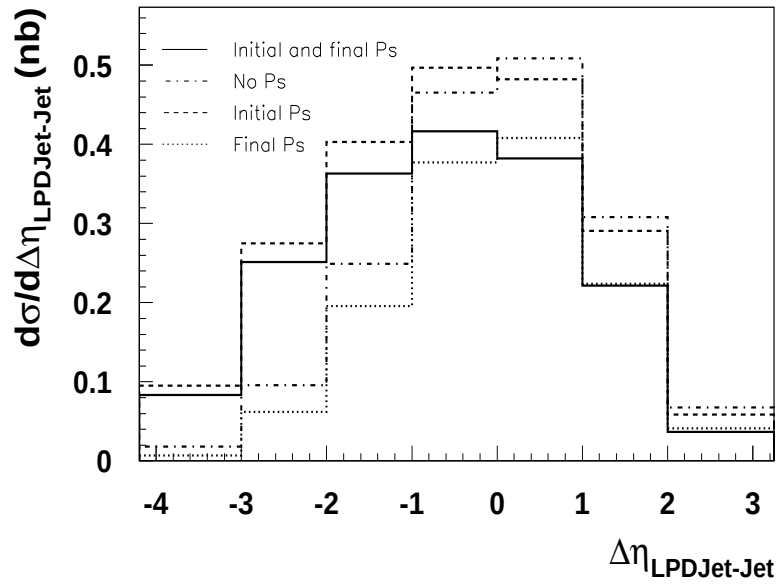

Figure 5.11: *Cross sections $d\sigma/d\Delta\eta_{LPDJet-Jet}$ for direct processes and different PS settings using the $CDF-CONE$ algorithm. Again we find some differences with Figure 5.3 but the conclusions remain the same.*

Cross sections were calculated for different processes using the K_t *algorithm* and it was shown that for resolved processes the mean value of $d\sigma/d\Delta\eta_{LPDJet-Jet}$ is shifted towards negative $\Delta\eta$. It was also shown that including PS the D^* cross section is larger for initial PS events than for initial and final PS in the selected region $P_t^{D^*} > 2\ GeV$. This is reflected in the differential cross sections as a function of $\eta_{LPDJet} - \eta_{Jet}$ as well as in the cross sections as a function of $P_t^{D^*}$.

Performing the analysis with the $CDF-CONE$ algorithm we arrived at the same conclusions. The difference in cross sections between the different jet algorithms is of the order of 15% for $R = 0.9$.

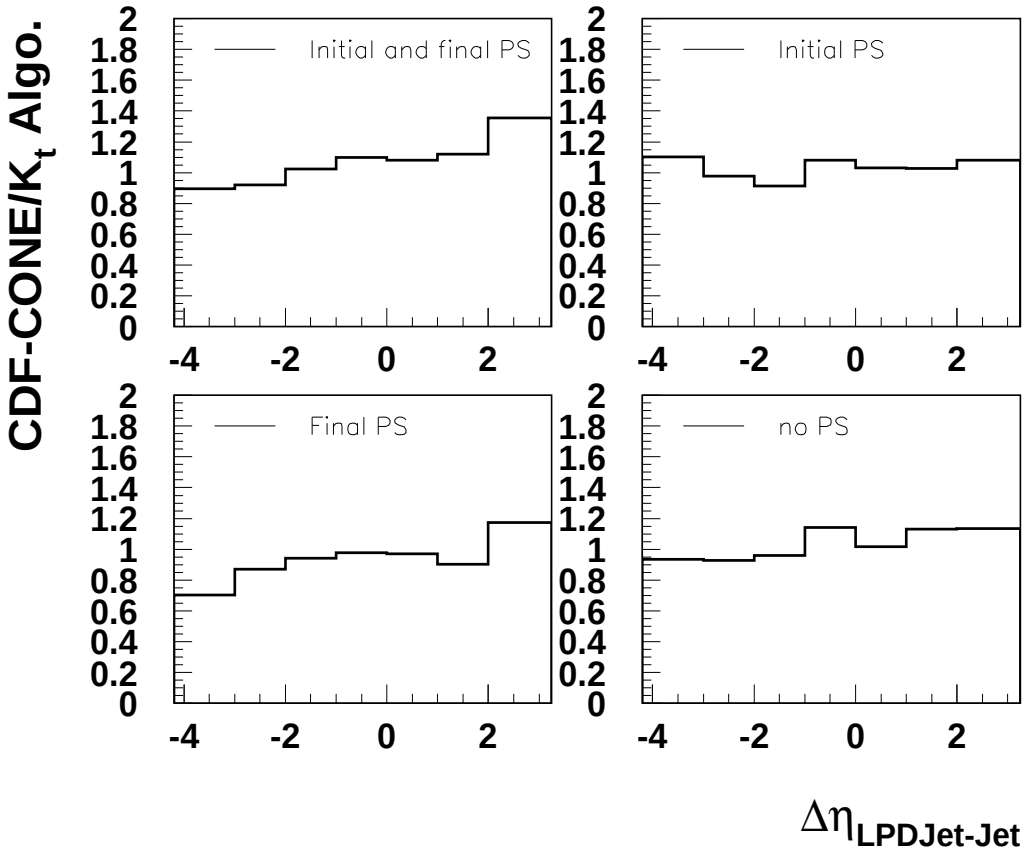

Figure 5.12: *Ratios between $CDF-CONE$ and K_t algorithm cross sections $d\sigma/d\Delta\eta_{LPDJet-Jet}$ for different PS settings.*

Chapter 6

RAPGAP vs PYTHIA comparison

The PYTHIA 6.2 [2] Monte Carlo generator offers the possibility of simulating Multiple Interaction events, MI, implementing several options, as discussed in section 2.4. This makes PYTHIA a very attractive tool and for this reason we want to have a comprehensive idea of the most important parameters that control the different steps in the event generator PYTHIA, i.e. initial and final state parton shower, PS, and hard scattering process. We change the paremeters one by one and study the effects on distributions of some kinematic variables: the photon virtuality, Q^2, the pseudo-rapidity, and transverse momentum P_t of the charm quarks. We will compare these distributions with the ones provided by RAPGAP 3.1 [1].

We focus mainly on the photoproduction regime, in this chapter defined as: $Q^2 < 1\ GeV^2$. Since we are not going to study hadronization, we have switched off any hadronization in the Monte Carlo event generators. We show a table with the parameters used in this chapter in table 6.1.

6.1 Direct processes.

6.1.1 The role of Q^2.

In figure 6.1 the differential cross section $d\sigma/dQ^2$ for the process $\gamma + g \rightarrow c\overline{c}$ as predicted from the RAPGAP and PYTHIA MC is shown. The charm quark mass is set to $m_c = 1.5\ GeV$ and $\sqrt{s} = 318\ GeV$ with $E_e = 27.5\ GeV$ and

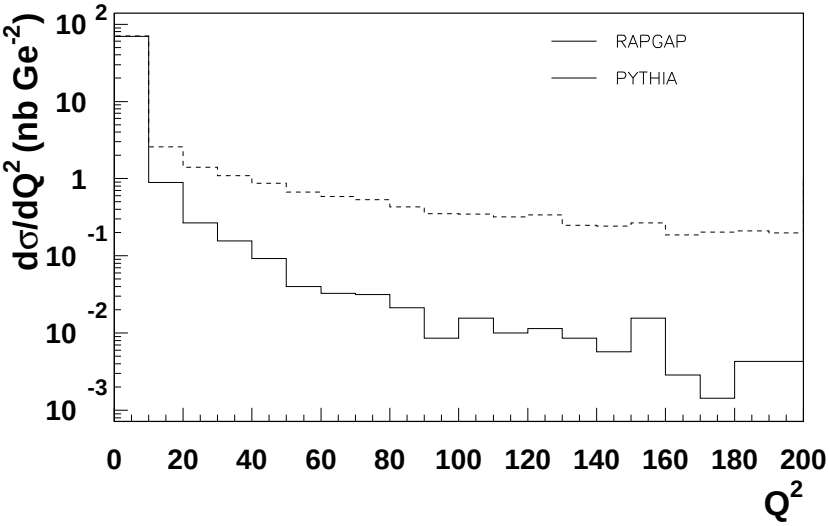

Figure 6.1: *Differential cross section, $d\sigma/dQ^2$. For $Q^2 < 10\ GeV^2$ we observe a good agreement between* RAPGAP *and* PYTHIA*, but for $Q^2 > 10\ GeV^2$ the* PYTHIA *cross section is always larger than* RAPGAP*.*

$E_p = 920\ GeV$, the electron and the proton energy beam. The maximum Q^2 value that will be produced in an event, Q^2_{max}, is set to the maximum kinematically allowed value and the minimum Q^2 value, Q^2_{min}, to zero. At this stage we switched off all kind of PS in order to compare only the hard processes, the parameters are shown in table 6.1. The effects of PS are studied in the next section.

In figure 6.1, we see two different regions: $0 < Q^2 < 10\ GeV^2$ and $10 < Q^2 < 200\ GeV^2$. In the first region the agreement between RAPGAP and PYTHIA seems to be perfect but in the second region the PYTHIA cross section is clearly above RAPGAP.

Figure 6.2a) shows the first region in more detail in the range $0 < Q^2 < 1\ GeV^2$. As before we see a quite good agreement between RAPGAP and PYTHIA with only some small fluctuations. In figure 6.2b) the ratio between RAPGAP and PYTHIA cross sections is shown. The deviations are less than 10% and within the errors consistent with one.

In figure 6.3 we show the differential cross section $d\sigma/dP_t^c$ with P_t^c being the transverse momentum of the charm quark in the laboratory frame. In figure 6.3a) we observe that the shape of the cross section is different in PYTHIA if we do not apply any cut on Q^2. If we apply the cut $Q^2 < 1\ GeV^2$

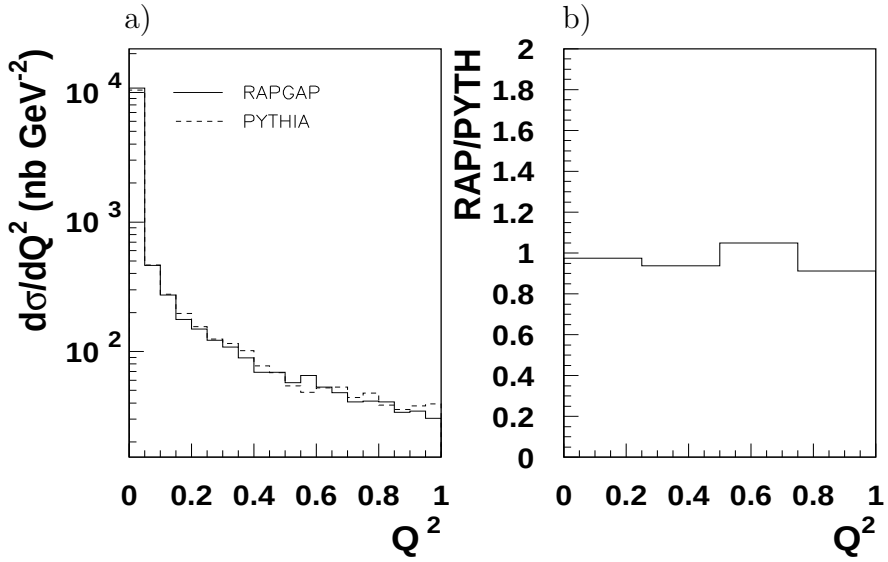

Figure 6.2: *On the left side the differential cross section, $d\sigma/dQ^2$ is shown in the Q^2 range: $Q^2 < 1\ GeV^2$ where we observe a good agreement between* Rapgap *and* Pythia*. On the right side is shown the ratio between the* Rapgap *and* Pythia *cross sections. The deviations are less than 10% and within the errors*

in Pythia, the shape of Pythia and Rapgap are similar. For Rapgap the shape is always the same although, as expected, the cross section is smaller when we cut for values where $Q^2 < 1\ GeV^2$. Figure 6.3b) shows the rate between Rapgap and Pythia cross sections, where we applied the cut $Q^2 < 1\ GeV^2$ for Pythia and Rapgap. We observe deviations about 20% within errors.

In figure 6.4 the cross section $d\sigma/d\eta_c$ is shown. In this case we have applied the cut $Q^2 < 1\ GeV^2$ and we find again a good agreement between Rapgap and Pythia. The right side shows the ratio between Rapgap and Pythia cross sections, where we also observe good agreement between both MC generators, at the level of $\sim$20%.

Since we are interested in the photoproduction region, $Q^2 < 1\ GeV^2$, and since the problematic region is situated in the region: $Q^2 > 10\ GeV^2$ we find acceptable agreement between the MC generators. In the following we restrict the Q^2 range to $Q^2 < 1\ GeV^2$.

Thus we conclude that Rapgap and Pythia agree on parton level at a 20%.

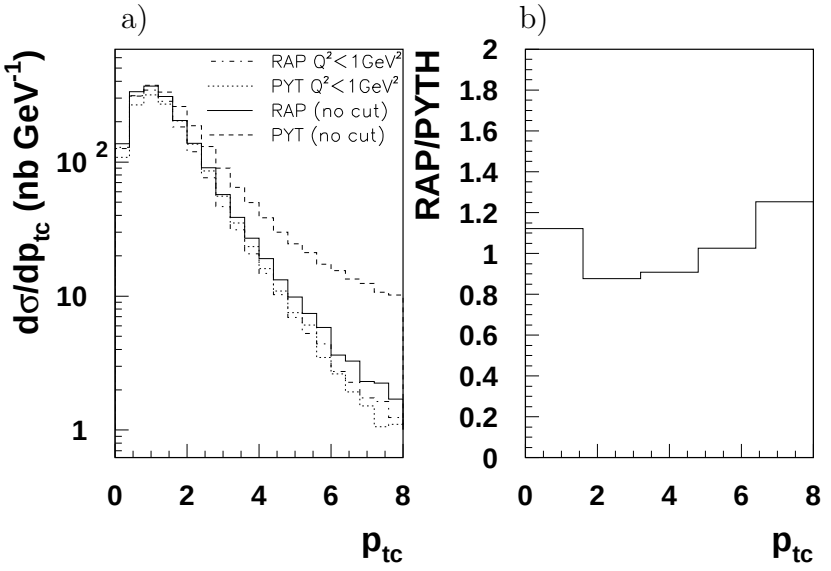

Figure 6.3: *On the left side is shown the differential cross section, $d\sigma/dP_t^c$. With the cuts $Q^2 < 1\ GeV^2$ we observe a good agreement between* RAPGAP *and* PYTHIA. *On the right side is shown the ratio between* RAPGAP *and* PYTHIA *cross sections where the cut $Q^2 < 1\ GeV^2$ is applied. The deviations are about 20% and within the errors.*

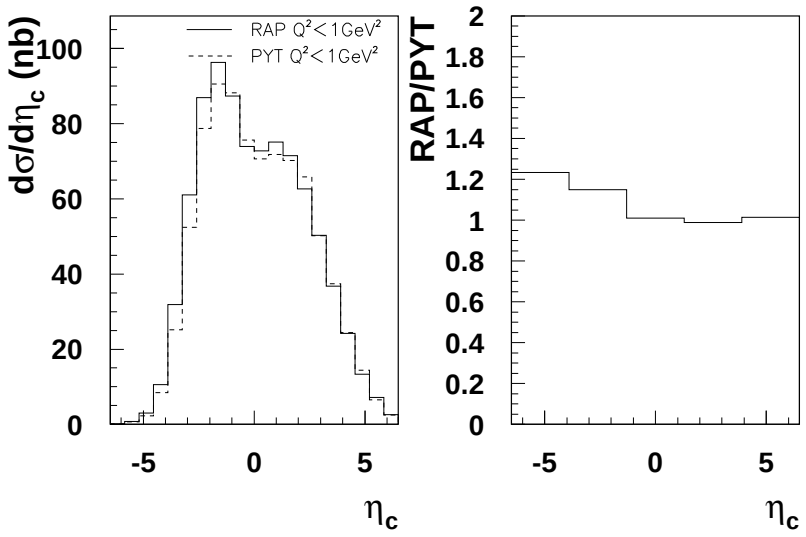

Figure 6.4: *On the left side the differential cross section, $d\sigma/d\eta_c$ is shown. With the cut $Q^2 < 1\ GeV^2$ we observe a good agreement between* RAPGAP *and* PYTHIA. *On the right side the ratio between* RAPGAP *and* PYTHIA *cross sections is shown where the cut $Q^2 < 1\ GeV^2$ is applied. The deviations from one are about 20%.*

6.1.2 Parton Shower.

In this section the different PS processes are studied in the region $Q^2 < 1\,GeV^2$. The MC generators provide information about the charm quarks before and after PS, but only the charm quarks after PS are investigated for the RAPGAP-PYTHIA comparisons, since they contain information about the PS process.

In Figures 6.5- 6.7 are shown the ratios between the RAPGAP and PYTHIA predictions for $d\sigma/dQ^2$, $d\sigma/d\eta_c$ and $d\sigma/dP_t^c$ cross sections respectively for final, initial, initial and final, and no PS events. In all four cases the deviations are below $\sim$20% within the errors.

In chapter 2 two factors of the PS approach were presented: the maximum parton virtuality and the QCD scale, Λ_{QCD}.

In RAPGAP and PYTHIA there are some predefinied hard interaction PS scale definitions, see table 6.1 and references [1] and [2]. In RAPGAP q^2_{max} is defined as:

$$q^2_{max} = Max(Q^2 + 2P_\gamma P_{q_1}, Q^2 + 2P_\gamma P_{q_2}) \tag{6.1}$$

whereas in PYTHIA it is:

$$q^2_{max} = p_t^2 + Q^2 + K_t^2 + m_c^2 + m_{\bar{c}}^2 \tag{6.2}$$

where P_γ is the four momentum of the photon, P_{q_1} the four momentum of one of the quarks in the hard interaction, Q^2 and K_t^2 are the virtualities of the photon and the gluon respectively, and m_c and $m_{\bar{c}}$ are the masses of the charm quark. Since we cannot change these definitions we are interested in the sensitivity of the event generator PYTHIA to changes of this scale. For this we applied in PYTHIA scale factors on the hard interaction scale for initial and final state PS. In figure 6.8a) the ratio RAPGAP PYTHIA is shown where the scale factors for both initial and final state PS were reduced in PYTHIA from 4 to 1. The default settings are also shown for comparison the changes. The differences are very small. If we look at the diagram involved, figure 2.4, we see that what we are doing by changing the maximum virtuality: before the hard scattering we are varying the K_t of the incoming gluon into the hard scattering with the initial state PS and after the hard scattering we are

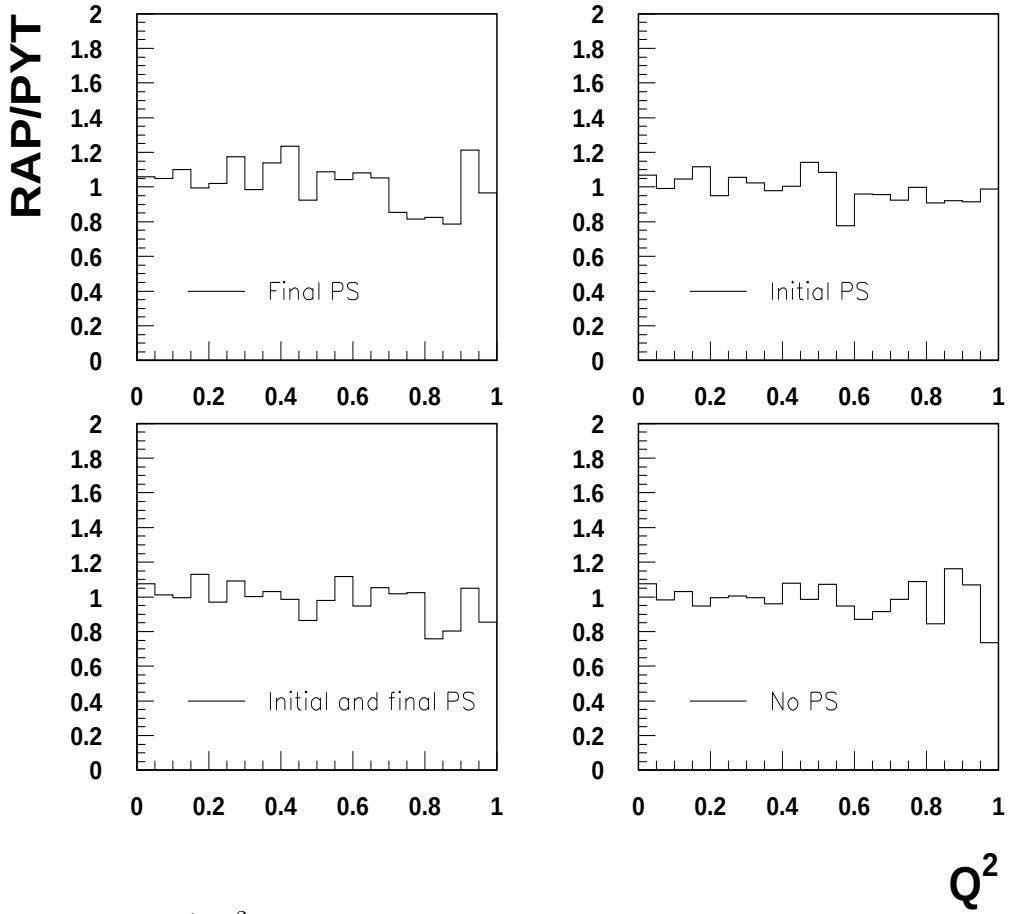

Figure 6.5: *$d\sigma/dQ^2$ cross section ratios between* RAPGAP *and* PYTHIA *are presented for initial, final, initial and final and no PS processes. The deviations are below 10% within the errors.*

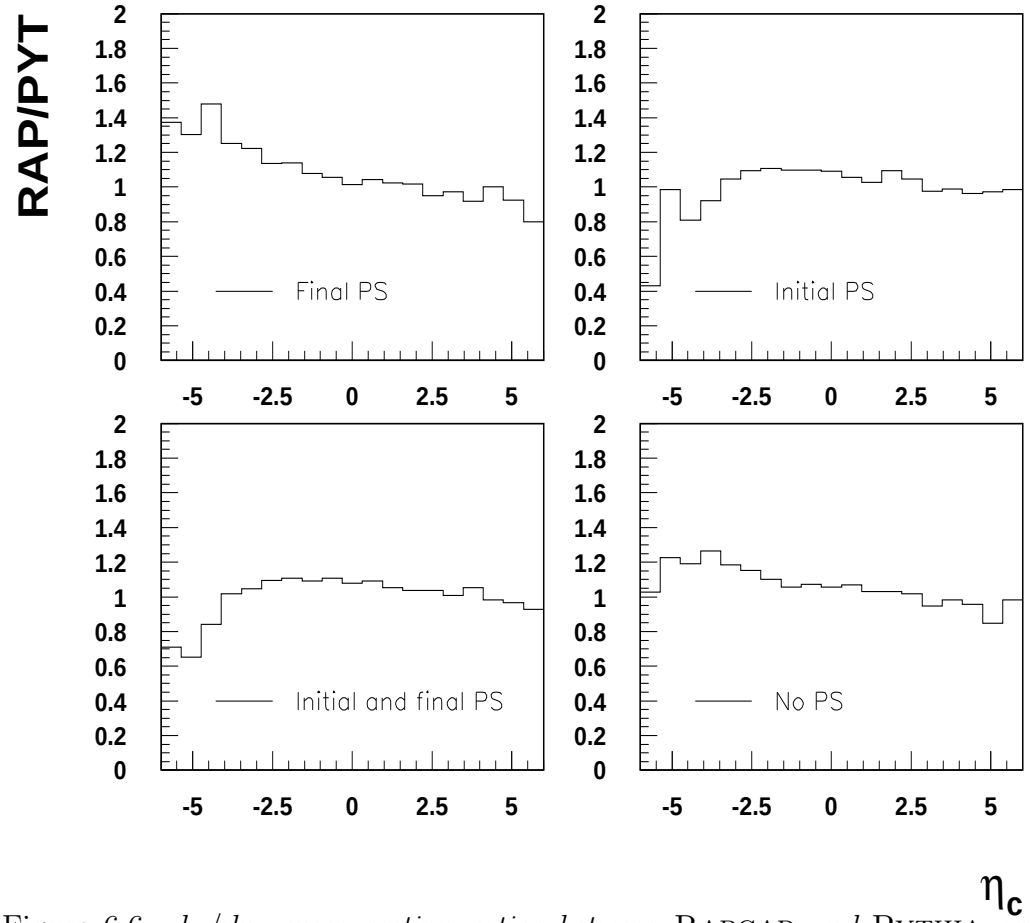

Figure 6.6: *$d\sigma/d\eta_c$ cross section ratios between* RAPGAP *and* PYTHIA *are presented for initial, final, initial and final and no PS processes. The deviations are below 10% within the errors.*

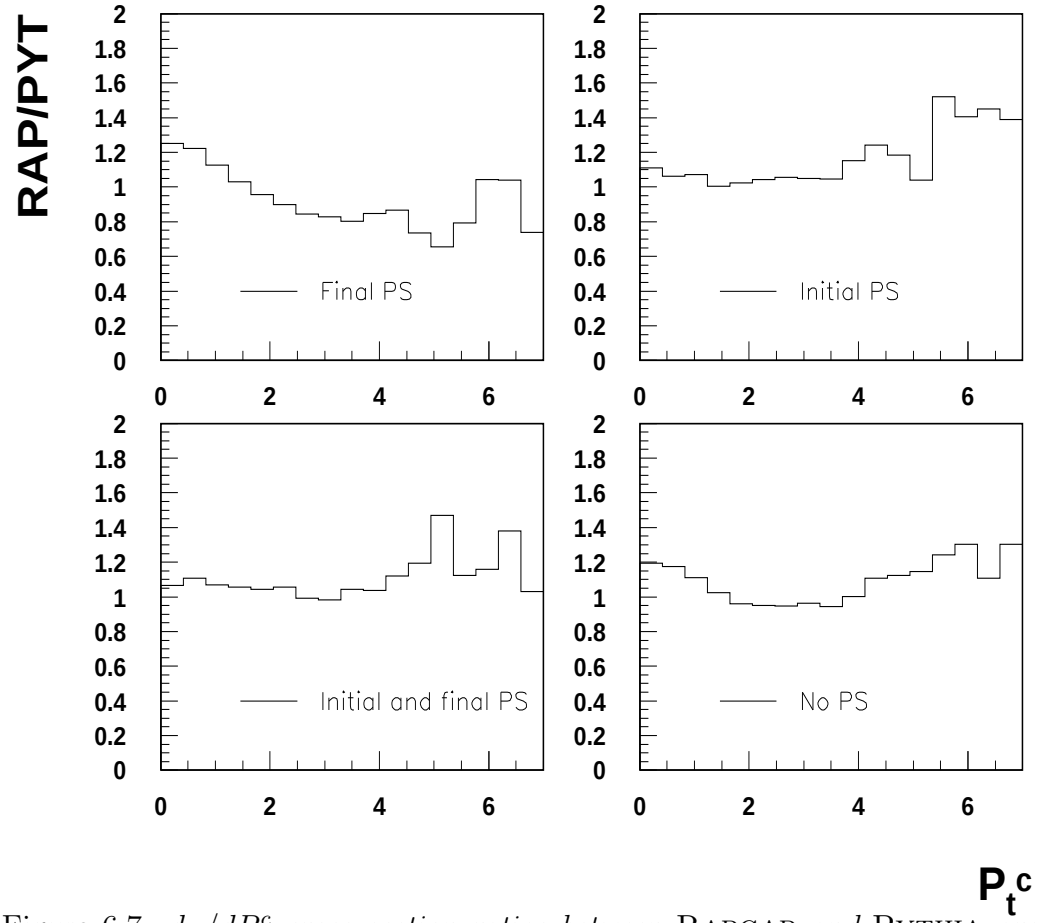

Figure 6.7: *$d\sigma/dP_t^c$ cross section ratios between* RAPGAP *and* PYTHIA *are presented for initial, final, initial and final and no PS processes. The deviations are below 10% within the errors.*

modifying the transverse momentum of the hard scattering outgoing partons with the final state PS. The reason for these small differences is that the influence of the maximum virtuality in the hard scattering process is limited in comparison with the hard scattering itself.

The default Λ_{QCD} values for the hard interaction, initial and final state PS are set in PYTHIA according to the parton distribution function parametrization. We can change them by setting the parameter MSTP 3 from 2 to 1 (this gives the user the control over the Λ_{QCD} values) and then changing them to the desired values, see table 6.1. Since we use the proton parton distribution function CTEQ 5L, we have been using $\Lambda_{QCD} = 0.192\ GeV$. In figure 6.8 b) are plotted the ratios between RAPGAP and PYTHIA using the value $\Lambda_{QCD} = 0.250\ GeV$ in initial and final state PS together with the default as a function of P_t^c. The changes in Λ_{QCD} in the PS has only little influence on the P_t of the charm quarks from the hard scattering.

In figure 6.8 c) we changed both the maximum virtuality, as in figure 6.8 a), and the Λ_{QCD}, as in figure 6.8 b) in the ratio RAPGAP with PYTHIA and compared it with the default settings. Again we do not see significant changes.

In Figure 6.9 a) the ratio RAPGAP with PYTHIA is shown with the combined changes of maximum virtuality and Λ_{QCD} as a function of η_c, and figures 6.9 b) and 6.9 c) represent the changes in the maximum virtuality and Λ_{QCD} respectively. Again the differences are small.

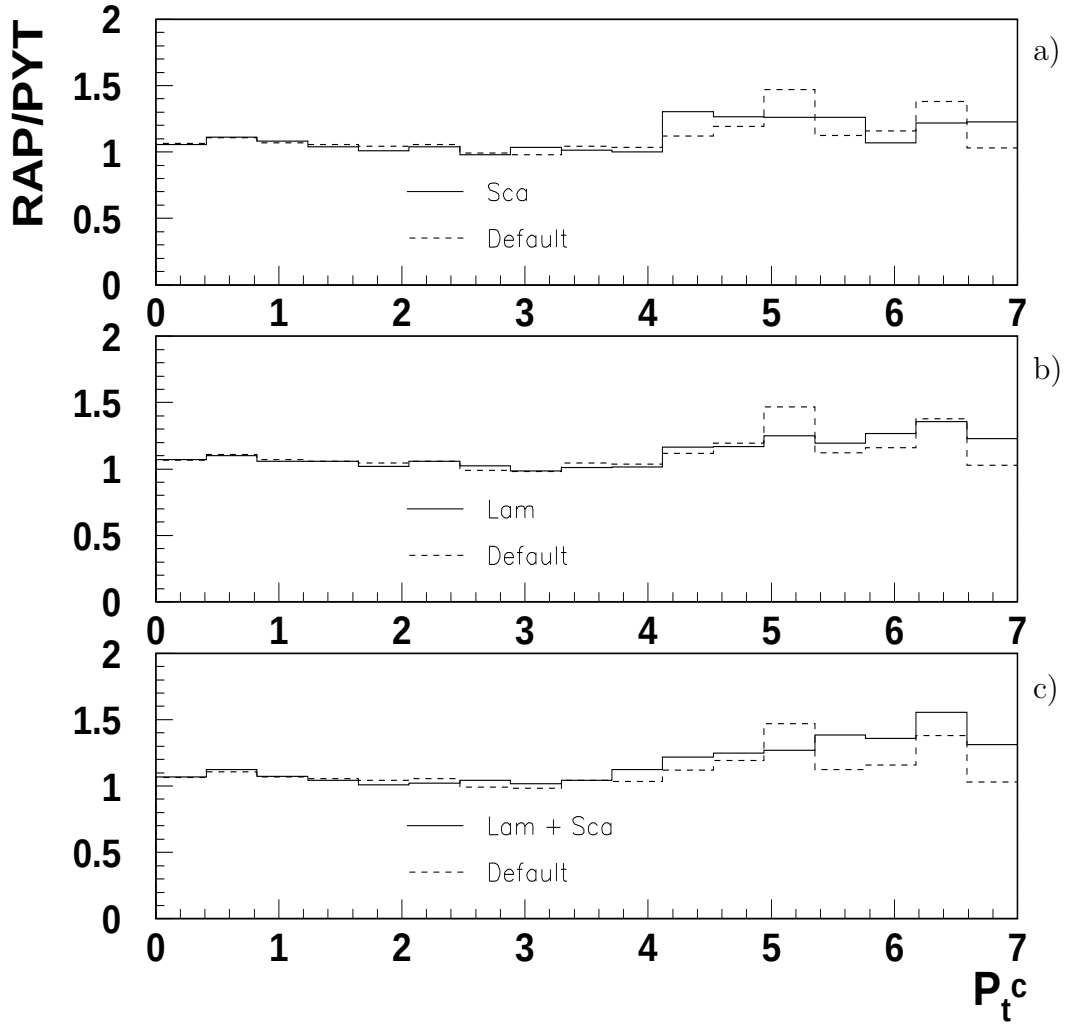

Figure 6.8: *$d\sigma/dP_t^c$ cross section ratios between* RAPGAP *and* PYTHIA *are shown where the Λ_{QCD} and the factor scales in initial and final state PS are changed. The deviations from the default settings are below 10% within errors.*

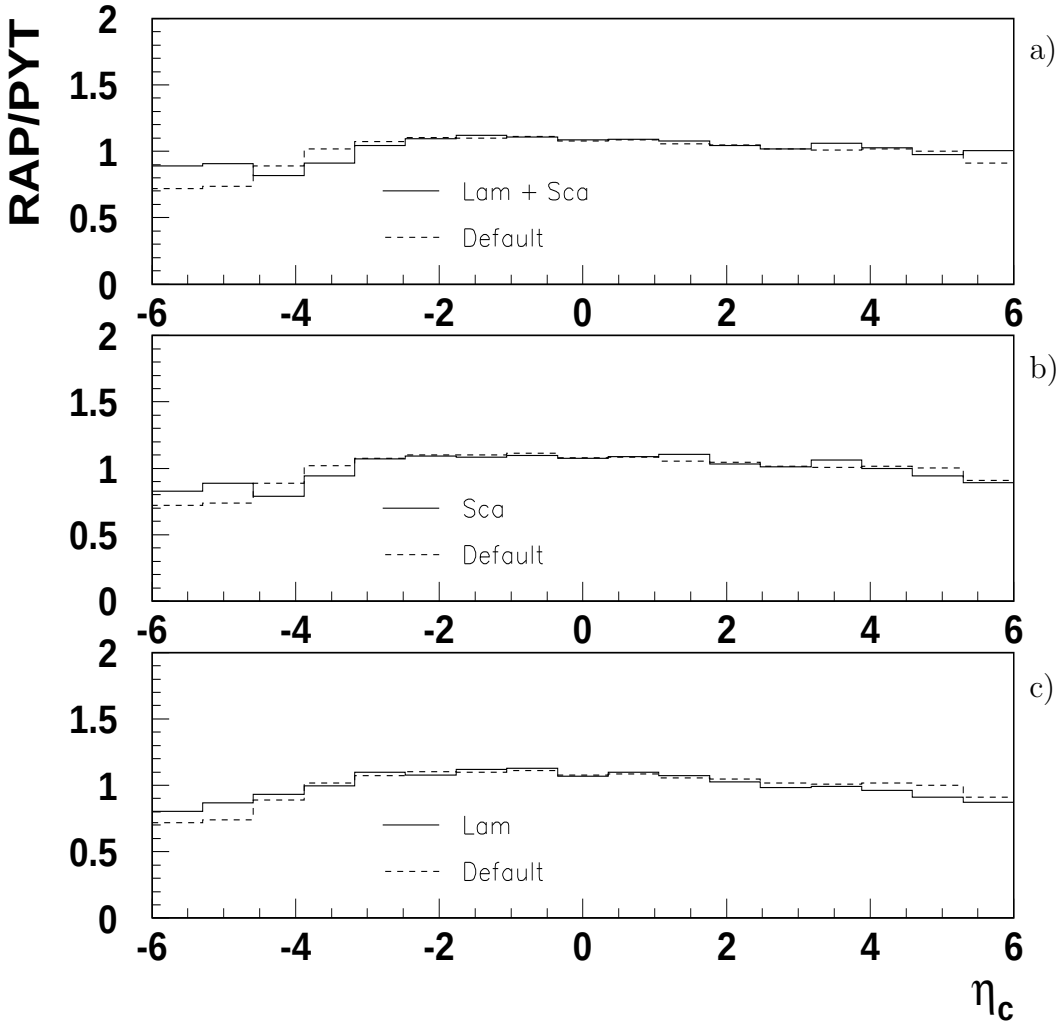

Figure 6.9: *$d\sigma/d\eta_c$ cross section ratios between* RAPGAP *and* PYTHIA *are shown where the Λ_{QCD} and the factor scales in initial and final state PS are changed. The deviations from the previous settings are below 10% within errors.*

	PYTHIA	RAPGAP	Short description
Q^2_{max}	CKIN 67	QMAX	lower Q^2 generation value
Q^2_{min}	CKIN 68	QMIN	upper Q^2 generation value
Hadronization	MSTP 111	NFRA	Hadronization master switch
PS	MSTP 61	IFPS	Inital state PS master switch
	MSTP 71	IFPS	Final state PS master switch
Hard scale	MSTP 32	IQ2S	Definition of the hard scattering scale
	PARP 67		Hard scattering scale factor in initial PS
	PARP 71		Hard scattering scale factor in final PS
Λ_{QCD}	MSTP 3		Λ_{QCD} from user or proton pdf
	PARP 61		initial PS Λ_{QCD} value
	PARP 71		final PS Λ_{QCD} value

Table 6.1: *The table shows some of the parameters that control the event generation in* PYTHIA.

Chapter 7

D^* Meson photoproduction.

In this chapter we present an analysis based on the D^* meson, inclusive and D^* jet production associated with a jet in photoproduction, i.e. $Q^2 < 0.01\ GeV^2$. The kinematic cut $0.29 < y < 0.65$ is applied, according to the acceptance of the electron tagger. In the analysis we used PYTHIA 6.2 [2] as Monte Carlo event generator. All the D^* particles in an event are treated independent of each other and of the decay mode. A D^* particle is identified in the *visible region* of: $P_t > 2\ GeV$ and $\mid \eta \mid < 1.5$, as in chapter 5 (see table 7.1).

In the first section we compare predictions to the measurement of [3]. The data were recorded with the H1 detector in 1999 and 2000 with an electron energy beam of 27.6 GeV and a proton energy beam of 920 GeV. The sources of the different errors are described in [3] and we present only the total errors.

We compare the results of the different charm jet selections: D^* Meson as Stable Particle (DSP) and the Leading Particle (LPD) methods.

7.1 D^* Meson Photoproduction.

In this section we present cross sections for inclusive D^* meson photoproduction and for D^* meson photoproduction associated with a jet, and we compare them with the data.

Q^2	$Q^2 < 0.01\ GeV^2$
y	$0.29 < y < 0.65$
η_{D^*}	$\mid \eta_{D^*} \mid < 1.5$
$P_t^{D^*}$	$P_t^{D^*} > 2\ GeV$
η_{Jet}	$\mid \eta_{Jet} \mid < 1.5$
P_t^{Jet}	$P_t^{Jet} > 3\ GeV$

Table 7.1: *In this table the cuts for y and Q^2 are defined as well as for D^* particles and jets (applied also for the D^*Jet).*

7.1.1 Inclusive D^* Photoproduction.

In the inclusive mode we identify the D^* particle in the *visible region*, i.e. independently of other possible event configurations. In figure 7.1 the differential cross section $d\sigma/dP_t^{D^*}$ is shown, where we stress that D^* means the D^* particle and not the D^*Jet. The contributions for direct, charm excitation and resolved photon events are added. In the region $2\ GeV < P_t^{D^*} < 3\ GeV$ the predicted cross section is clearly larger than data, whereas in the large $P_t^{D^*}$ range the cross section describes the measurements.

In figure 7.2 the differential cross section $d\sigma/d\eta_{D^*}$ is presented. The predictions in the backward region, $\eta < 0$, is larger than data. An hypothesis that could explain the overestimation in the small $P_t^{D^*}$ and backward regions is that the charm quarks are treated as massless quarks in the charm excitation contribution. At low transverse momentum the effect of the charm mass can be large enough to become important in the calculations compared to the data.

7.1.2 D^* Meson Production Associated with a Jet.

In this case, in addition to the D^*, we require 2 jets, $1D^*Jet + 1Jet$. One of the jets is the D^* Jet, where we use the D^* Meson as Stable Particle and the K_t *algorithm*, as described in chapter 3. This is done in order to be able to compare these calculations to the data of [3]. The jets, also the D^*Jet,

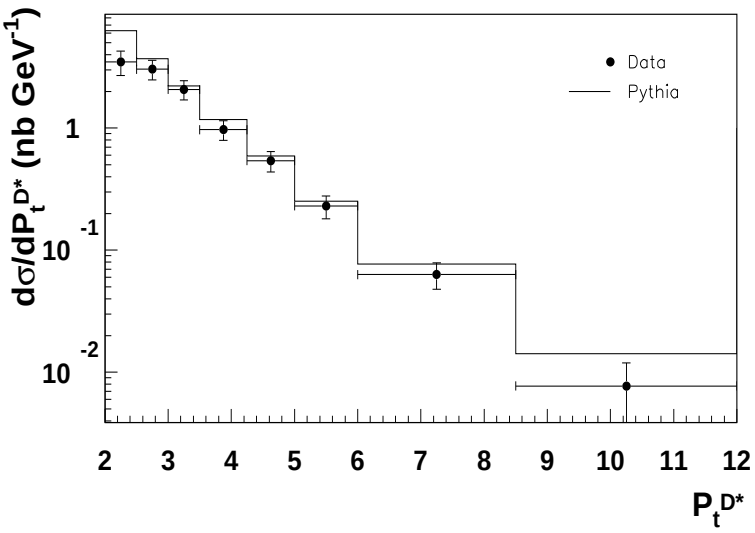

Figure 7.1: *Differential cross section $d\sigma/dP_t^{D^*}$. The contributions from direct, charm excitation and resolved photon events are added and compared to the data.*

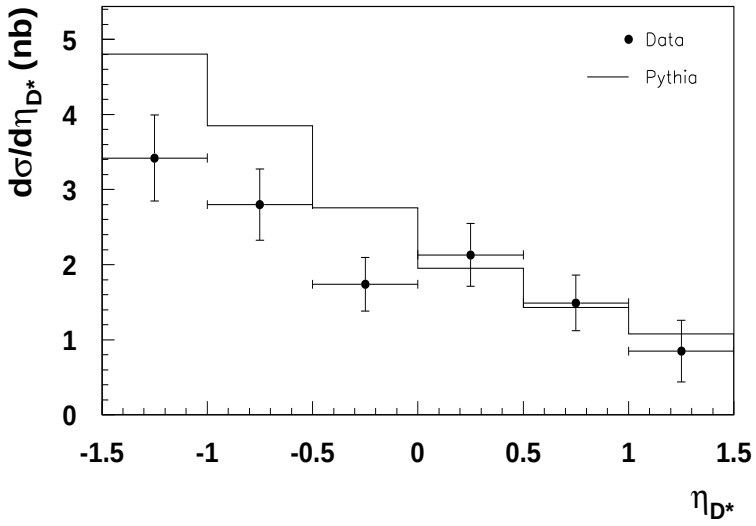

Figure 7.2: *Differential cross section $d\sigma/d\eta_{D^*}$. The contributions for direct, charm excitation and resolved photon events are shown and compared to the data.*

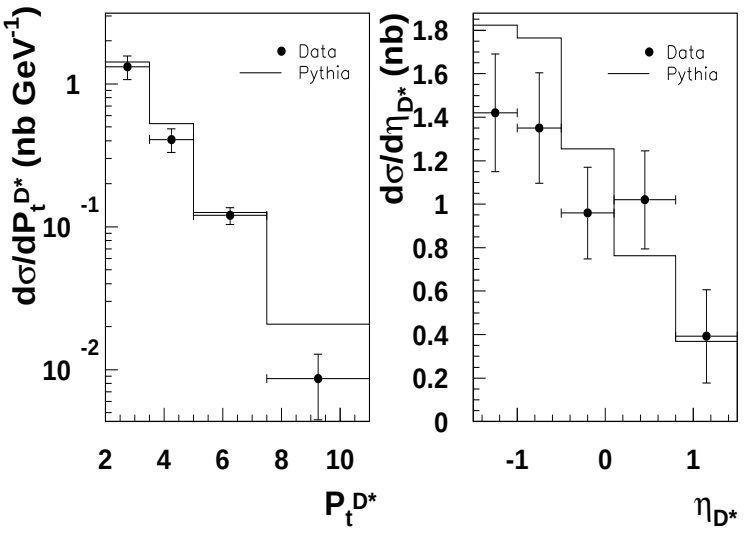

Figure 7.3: *Differential cross sections $d\sigma/dP_t^{D^*}$ and $d\sigma/d\eta_{D^*}$ for $1D^*Jet + 1Jet$ configuration events. The contributions from direct, charm excitation and resolved photon events are added and compared to data.*

are required to fulfil the cuts: $P_t > 3\ GeV$ and $\mid \eta \mid < 1.5$. If we find more than one jet we take into account only the jet with highest P_t. The cuts are summarized in table 7.1.

In figure 7.3 the differential cross sections of D^* meson $d\sigma/dP_t^{D^*}$ and $d\sigma/d\eta_{D^*}$ are presented. The P_t^{D*} and η_{D^*} distributions are more or less well described within the experimental errors.

Figure 7.4 shows the differential cross sections $d\sigma/dP_t^{Jet}$ and $d\sigma/d\eta_{Jet}$. In this case the predictions fit better the data, especially the differential cross section as a funtion of P_t^{Jet}. The η_{Jet} distribution fits the data within errors in the forward region, $\eta > 0$, but in the backward region the predictions tends to overshoot the measurements, although they are still compatible within errors.

7.2 D^* Meson as Stable Particle vs Leading Particle Methods.

In this section we study the differences in the analysis from the charm jet selection methods: D^* Meson as Stable Particle and Leading Particle.

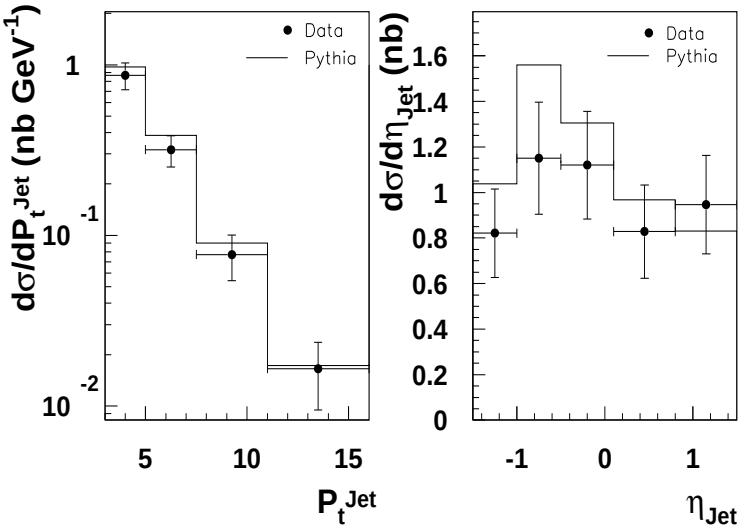

Figure 7.4: *Differential cross sections $d\sigma/dP_t^{Jet}$ and $d\sigma/d\eta_{Jet}$ for $1D^*Jet + 1Jet$ configuration events. The contributions from direct, charm excitation and resolved photon events are added and compared to data.*

In figure 7.5 the differential cross sections $d\sigma/dP_t^{D^*}$ and $d\sigma/d\eta_{D^*}$ are shown for both methods in $1D^*Jet + 1Jet$ events. In figure 7.5 a) we see that the larger differences are in the smaller tranverse momentum region, $2\ GeV < P_t^{D^*} < 3.5\ GeV$. This can be understood since for small $P_t^{D^*}$, the D^* transverse momenta of the decay particles can become comparable to $P_t^{D^*}$. If this happens and the direction of the Leading Particle is different from the direction of the D^* particle we get different results (see figure 5.7).

Figure 7.5 b) shows that the larger differences are in the backward region, which corresponds again to the lower $P_t^{D^*}$.

In figure 7.6 we present the differential cross sections $d\sigma/dP_t^{Jet}$ and $d\sigma/d\eta_{Jet}$. Again both methods agree for large P_t^{Jet} but we find discrepancies in the low P_t^{Jet} region. In the η_{Jet} distribution we see only small discrepancies, about 10%.

It could be interesting to do the same analysis with data using the LPD method and compare it to our predictions. It could be possible that the data and the predictions, due to the different behaviour at low P_t (see figures 7.3 and 7.4) would agree better in comparison with the DSP method.

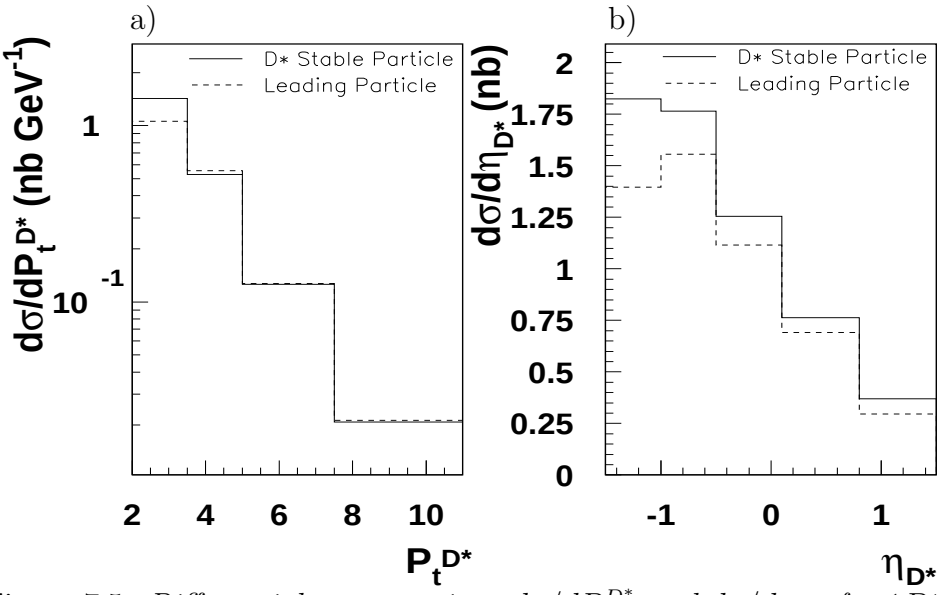

Figure 7.5: *Differential cross sections $d\sigma/dP_t^{D^*}$ and $d\sigma/d\eta_{D^*}$ for $1D^*Jet + 1Jet$ configuration events. The contributions from direct, charm excitation and resolved photon events are added. The charm jet selection methods: DSP and LPD compared. The larger differences are due to slow D^* particles.*

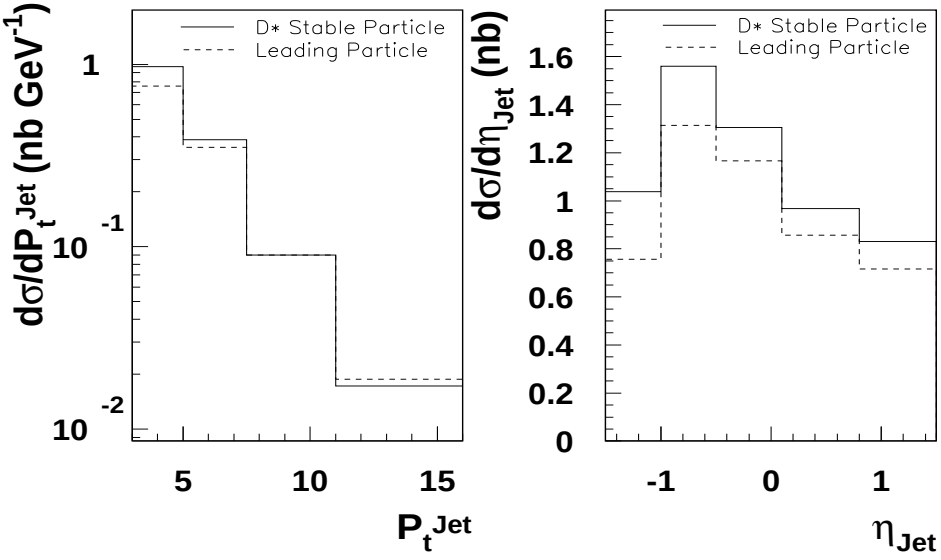

Figure 7.6: *Differential cross sections $d\sigma/dP_t^{Jet}$ and $d\sigma/d\eta_{Jet}$ for $1D^*Jet + 1Jet$ configuration events. The contributions from direct, charm excitation and resolved photon events are added. The charm jet selection methods: DSP and LPD compared.*

In this chapter we introduced a D^* Meson photoproduction study using PYTHIA without MI. We saw that the predictions describe fairly well the data. In the next chapter we will include PYTHIA with MI to see if the MI model can improve the description of the cross sections.

We also compared the K_t and the $CDF - CONE$ algorithms and saw that at large P_t both algorithms converge. We have also studied a calibration of the K_t and the $CDF - CONE$ algorithms with the charm jet selections methods: Leading Particle and D^* Meson as Stable Particle, not shown in the thesis. We found that the methods combined with any of the algorithms converge at large P_t.

Chapter 8

Multiple Interactions.

In the previous chapter we presented cross sections of events with a D^* particle in the *visible region* and the $1D^*Jet + 1Jet$ configuration as a function of $P_t^{D^*}$, P_tJet, η_{D^*} and η_{Jet} and we compared them to the data.

In the first section of this chapter we present also cross sections of events with a D^* in the *visible region* and the $1D^*Jet + 1Jet$ configuration but now including the MI model introduced in section 2.4. We compare them also to the measurements of [3].

Next we search for clear signatures, sensitive to MI, in heavy photoproduction. The analysis is done only at Monte Carlo level, using PYTHIA, and no data are presented.

As in the previous chapters, the charm production is tagged by a D^* particle and the D^*Jet. The cuts for the D^* particle, the D^*Jet and the jets are in table 7.1. using the K_t algorithm.

8.1 D^* Meson Photoproduction and Multiple Interactions.

In this section we present a comparison of the different Multiple Interactions, MI, options in PYTHIA. We use the heavy quark selection as presented in section 7.1, i.e. basically the charm jet selection D^* Meson as a Stable

Particle, the K_t algorithm with the cuts in table 7.1. The different options for MI are collected in table 2.1 (note the abbreviation column).

We also present a comparison of the MI model and the data. At the end, we include the CDF tune for the double Gaussian MI option, MI-4, in the comparison. This CDF tune is a set of parameters for MI obtained at the Collider Detector at Fermilab and has been parametrized for pp collisions at 630 GeV and 1.8 TeV to describe the "*underlying event*". Both the default mode values and the CDF tune are in table 8.1.

The aim is to investigate possible signals and effects coming from MI in the measurements already available. We also want to see if one can already conclude from a comparison with the data whether MI in heavy quark production is relevant at HERA.

8.1.1 Inclusive D^* photoproduction and Multiple Interactions.

Figure 8.1 shows the differential cross sections $d\sigma/dP_t^{D^*}$ and $d\sigma/d\eta_{D^*}$ for D^* photoproduction in the *visible range*, where the contributions from direct, charm excitation and resolved photon events are added. We see that the two options of the MI model with an impact parameter, MI-3 and MI-4, have similar cross sections and are larger than the other. We see also that the differences are roughly independent of $P_t^{D^*}$. In MI-1 and MI-2, where all the events have the same MI probability, the cross sections are similar and we see no significant differences in using an abrupt $p_{\perp min}$ cut or a continuous one. In MI-3 and MI-4, the options with an impact parameter, we also see no large differences in the cross sections.

8.1.2 D^* Meson Production Associated with a Jet and Multiple Interactions.

In figure 8.2 the differential cross sections $d\sigma/dP_t^{D^*}$ and $d\sigma/d\eta_{D^*}$ for $1D^*Jet+1Jet$ configuration with the four MI options are shown. We also see similar cross sections for MI-1 and MI-2, and for MI-3 and MI-4.

Figure 8.3 shows the differential cross sections $d\sigma/dP_t^{Jet}$ and $d\sigma/d\eta_{Jet}$. Again we find the same grouping between options but here we see a different shape of the η distributions.

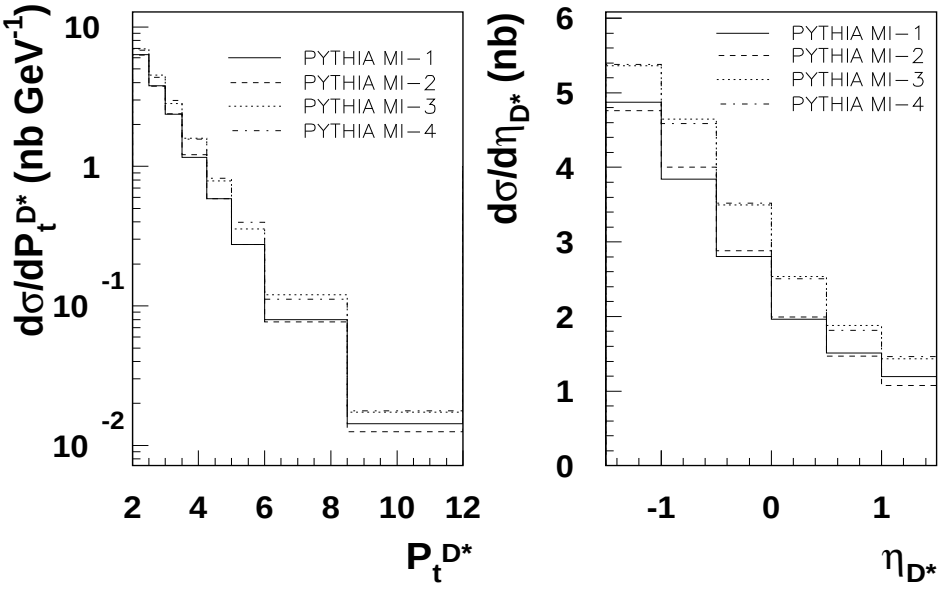

Figure 8.1: *Differential cross sections $d\sigma/dP_t^{D^*}$ and $d\sigma/d\eta_{D^*}$ in inclusive D^* photoproduction. The contributions from direct, charm excitation and resolved photon events, including the MI, are added.*

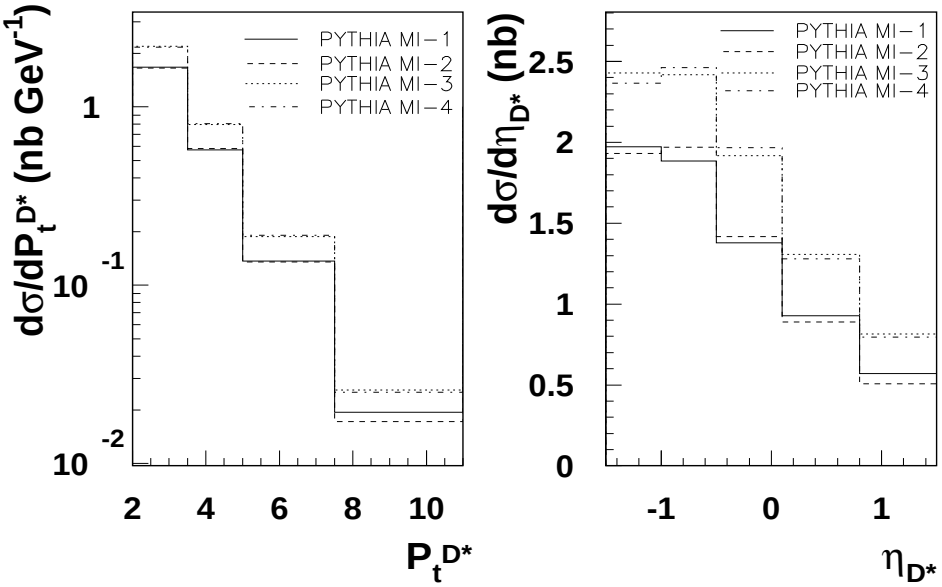

Figure 8.2: *Differential cross sections $d\sigma/dP_t^{D^*}$ and $d\sigma/d\eta_{D^*}$ for $1D^*Jet + 1Jet$ configuration events. The contributions from direct, charm excitation and resolved photon events, including the MI, are added.*

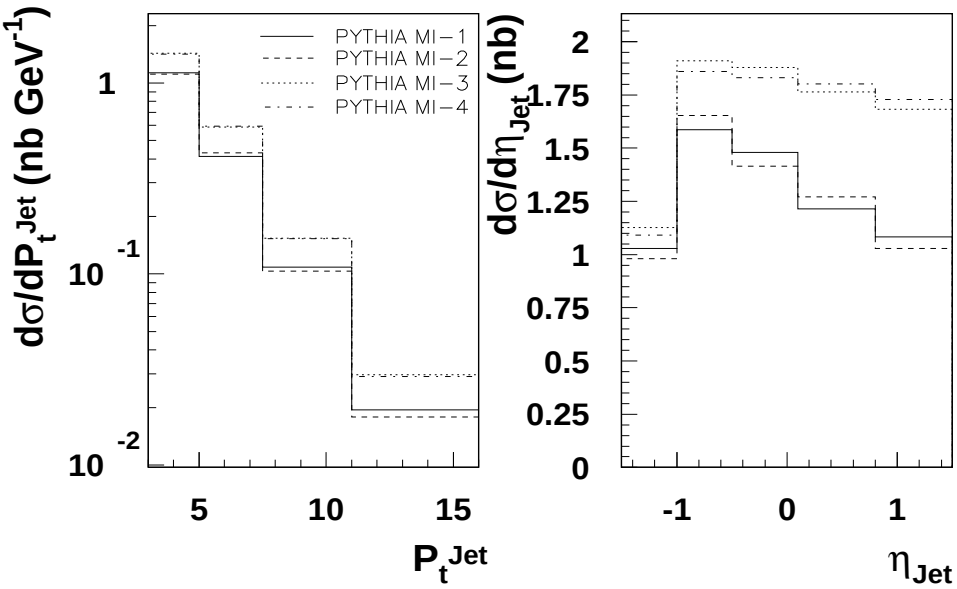

Figure 8.3: *Differential cross sections $d\sigma/dP_t^{Jet}$ and $d\sigma/d\eta_{Jet}$ for the $1D^*Jet+1Jet$ configuration. The contributions from direct, charm excitation and resolved photon events, including the MI, are added.*

8.1.3 Comparison to data.

Here we used MI-2 and MI-4 to compare to the data since the other options give already identical results. The aim of this comparison is to check the consistency of the model prediction with the data. It is clear from the beginning that the measurements available here are not designed to be sensitive to MI and therefore might show only small discriminative power.

Figure 8.4 shows the differential cross sections $d\sigma/dP_t^{D^*}$ and $d\sigma/d\eta_{D^*}$ of D^* photoprodduction in the *visible range*. The charm excitation components are also shown. In general, the MI models overestimate the cross sections, also at large $P_t^{D^*}$ in contrast to the previous calculations in section 7.1. This is especially true for MI-4, option with an impact parameter and a double Gaussian matter distribution. The reason can be again the massless calculations for the excitation contribution in PYTHIA. However it is interesting to note that the shapes of the $P_t^{D^*}$ and η_{D^*} distributions are not affected by MI.

Figure 8.5 shows the differential cross sections $d\sigma/dP_t^{D^*}$ and $d\sigma/d\eta_{D^*}$, for

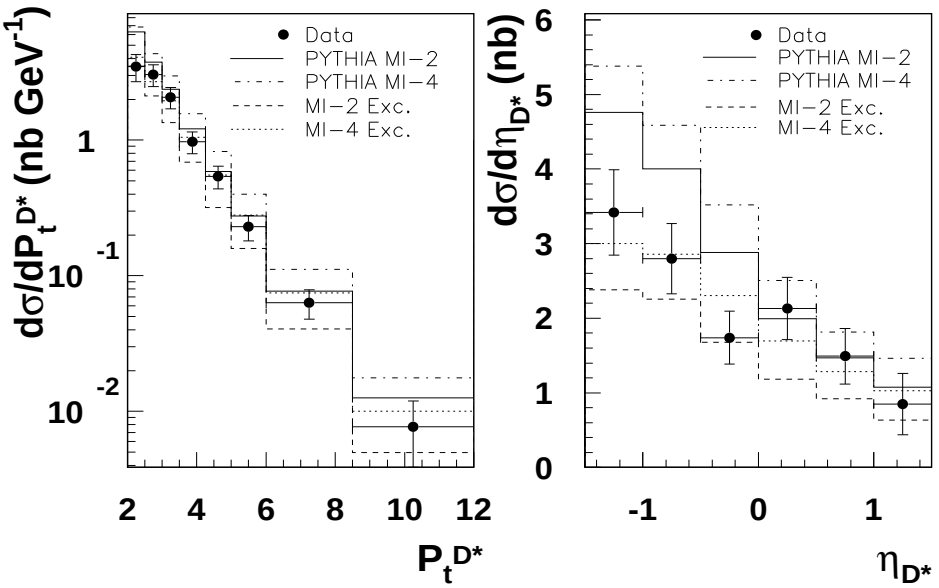

Figure 8.4: *Differential cross sections $d\sigma/dP_t^{D^*}$ and $d\sigma/d\eta_{D^*}$ in inclusive D^* photoproduction. The contributions from direct, charm excitation and resolved photon events, including the MI, are added and compared to data.*

the $1D^*Jet+1Jet$ configuration. As well as in inclusive D^* photoproduction, here we see that the MI model overestimates the cross sections, especially MI-4. This is again here roughly independent of $P_t^{D^*}$.

In figure 8.6 the differential cross sections $d\sigma/dP_t^{Jet}$ and $d\sigma/d\eta_{Jet}$ are shown. The MI overestimate again $d\sigma/dP_t^{Jet}$ independently of P_t^{Jet} and the difference in the cross section $d\sigma/d\eta_{Jet}$ is now very large for $\eta_{Jet} > -1$. It is interesting again to note that the shape of the η_{Jet} distribution, although very different between the two MI approaches, is still consistent with the measurements. It would be also interesting to extend the measurements to larger η_{Jet}. There the differences are expected to be larger and we could see if the shape decreases slowly, as proposed by MI-4, or strongly, as shown by PYTHIA without MI or MI-2. We note that the component charm excitation in MI-4 is responsible of this change of shape in the $d\sigma/d\eta_{Jet}$ cross section.

In figure 8.7 the cross sections $d\sigma/dP_t^{D^*}$ and $d\sigma/d\eta_{D^*}$ in inclusive D^* photoproduction are shown. The $CDF\ Tune$ is compared with the $MI-4\ Default$. The differences in $P_t^{D^*}$ are very small and are very difficult to distinguish, whereas for η_{D^*} larger differences arise in the regions $\mid \eta_{D^*} \mid > 0.5$,

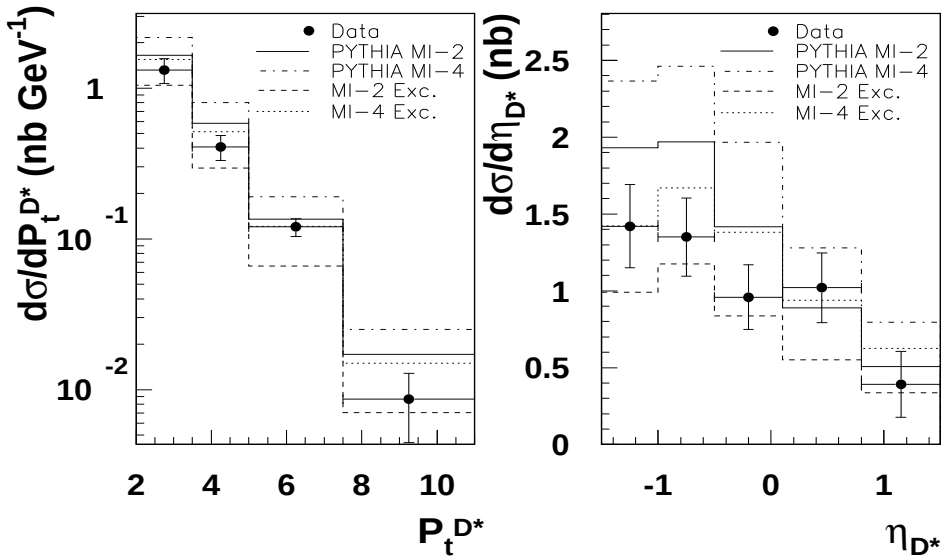

Figure 8.5: *Differential cross sections $d\sigma/dP_t^{D^*}$ and $d\sigma/d\eta_{D^*}$ for the $1D^*Jet + 1Jet$ configuration. The contributions from direct, charm excitation and resolved photon events, including the MI, are added and compared to data.*

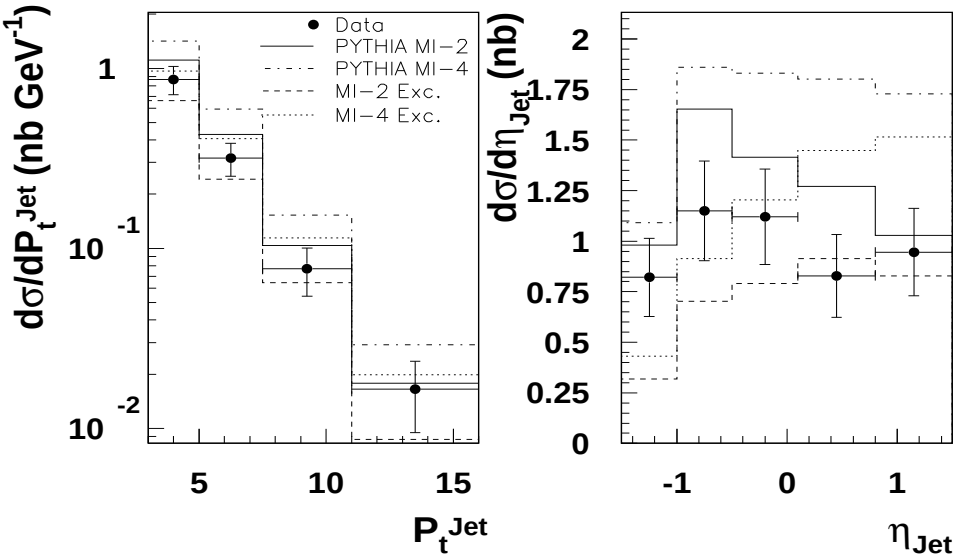

Figure 8.6: *Differential cross sections $d\sigma/dP_t^{Jet}$ and $d\sigma/d\eta_{Jet}$ for the $1D^*Jet + 1Jet$ configuration. The contributions from direct, charm excitation and resolved photon events, including the MI, are added and compared to data. The legend is the same for both cross sections.*

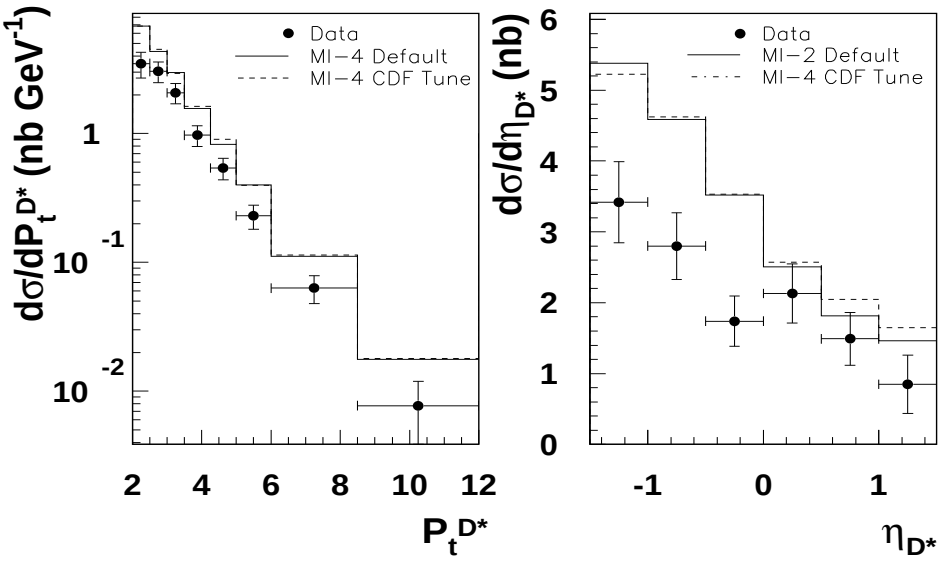

Figure 8.7: *Differential cross sections $d\sigma/dP_t^{D^*}$ and $d\sigma/d\eta_{D^*}$ in inclusive D^* photoproduction. The contributions from direct, charm excitation and resolved photon events, are added for MI-2 and the CDF Tune and compared to data.*

i.e. there are no changes in the very central region.

Figure 8.8 shows the cross sections $d\sigma/dP_t^{D^*}$ and $d\sigma/d\eta_{D^*}$ for $1D^*Jet + 1Jet$ events. In this case we see slightly larger differences between the two sets of parameters, but the shapes remain the same as before. In figure 8.9 the cross sections $d\sigma/dP_t^{Jet}$ and $d\sigma/d\eta_{Jet}$ for $1D^*Jet+1Jet$ events are shown. In this case we see a different behaviour in the $\eta > 0$ region: MI-4 Default shows a decreasing cross section with η whereas with the MI-4 CDF-Tune the cross section increases.

We have seen that the shapes provided by the MI model are compatible with the measurements and that could even give a better description in some cases. As PYTHIA is using Leading order matrix elements, the normalization might change by changing scales in α_s. After this section it is not evident that in *ep* collisions MI play a role although in *pp* collisions they do, see [25].

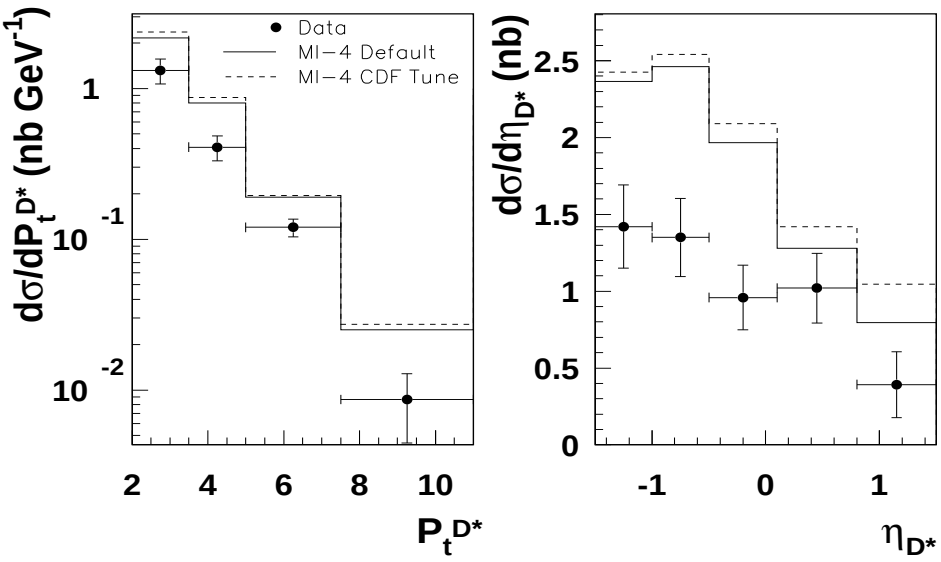

Figure 8.8: *Differential cross sections $d\sigma/dP_t^{D^*}$ and $d\sigma/d\eta_{D^*}$ for the $1D^*Jet + 1Jet$ configuration. The contributions from direct, charm excitation and resolved photon events, are added for MI-4 Default and the CDF Tune and compared to data. The legend is the same for both cross sections.*

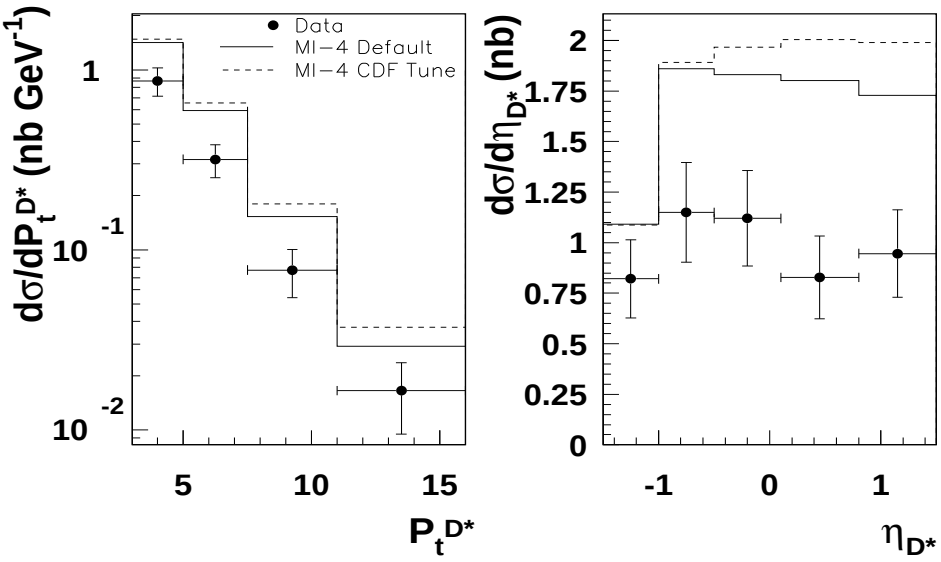

Figure 8.9: *Differential cross sections $d\sigma/dP_t^{Jet}$ and $d\sigma/d\eta_{Jet}$ for the $1D^*Jet + 1Jet$ configuration. The contributions from direct, charm excitation and resolved photon events, are added for MI-4 Default and the CDF Tune and compared to data. The legend is the same for both cross sections.*

Parameter PARP	Default value	CDF Tune [1]
81	1.90 GeV	not used
82	1.9 GeV	2.0 GeV
83	0.5	0.5
84	0.2	0.4
85	0.33	0.9
89	1,000.0 GeV	1,800.0 GeV
90	0.16	0.25

Table 8.1: *Summary of the default parameters relevant for MI in* PYTHIA *(see also table 2.1).*

8.2 The Transverse Region and Multiplicity.

In the previous section we began exploring the features of the MI model and its options. There we presented an analysis based on events with a D^* particle in the *visible region* and the $1D^*Jet + 1Jet$ configuration and presented cross sections as a function of $P_t^{D^*}$, P_tJet, η_{D^*} and η_{Jet} and saw that the predicted cross sections using MI are larger than the data but that the shapes are different and could be compared to the data.

In this section we present two important concepts in the analysis to study MI: the transverse region and multiplicity.

The *tranverse region* has been proven to be sensitive to MI in pp collisions, see [25], and is shown in figure 8.10. The D^*Jet defines a reference axis. We define three regions relative to this axis: toward, away and transverse. These regions are defined as: toward in $\mid \phi \mid < 50$, away in $\mid \phi \mid > 100$ and the transverse in $50 < \mid \phi \mid < 100$.

Multiplicity is defined as the average number of particles measured per event. In this analysis the particles are always measured in the region $\mid \eta \mid < 1.5$ and the transverse momentum of the particles in the laboratory frame fulfil $P_t > 0.5\ GeV$.

.

[1]The CDF Tune also includes: PARP 67 = 4.0, see table 6.1

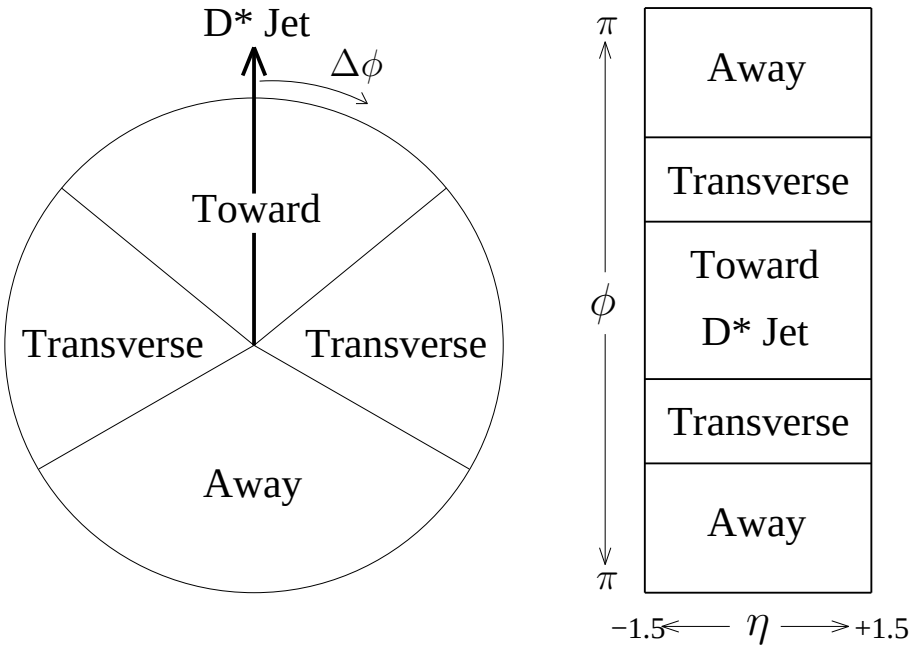

Figure 8.10: *Toward, away and transverse regions defined in the $\eta - \phi$ space taking the D^*Jet as reference.*

8.3 Regions in $1D^*Jet + 1Jet$ events.

In this section we study the most immediate properties of the toward, away and transverse regions in $1D^*Jet + 1Jet$ events, where we use only the LPD Charm Jet Selection.

Figure 8.11 shows the multiplicity as a function of ϕ, as defined in figure 8.10, for direct, resolved and charm excitation components whithout including MI. Here we can see very clear the three regions, from left to right: toward, transverse and away.

In the toward region, by definition, we have the D^*Jet, whereas the second jet is in the away region, due to momentum conservation since these jets are created in the hard scattering. In the toward region we see a sharp peak, with a width of about 40 degrees, whereas the peak in the away region is lower but with a width of about 60 degrees. The widths are different because the two jets, the D^*Jet and the Jet, are not exactly back-to-back. It may be also important that these two jets contain different sort of hadrons.

The transverse region is characterized by a very low activity for all the contributions, since the particles in this region come from the initial and final state parton shower. In the transverse region the largest contribution comes form the direct processes. In figure 5.1b) we see that in direct processes

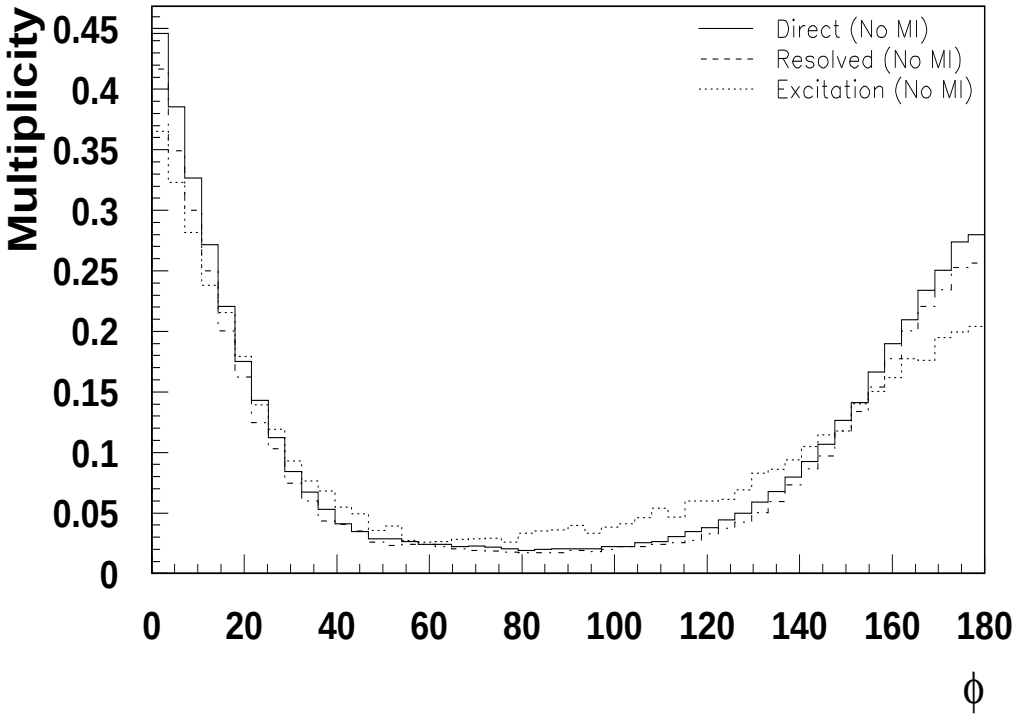

Figure 8.11: *Multiplicity as a function of ϕ for the direct, resolved and charm excitation components in $1D^*Jet + 1Jet$ events. The three regions: toward, away and transverse are clearly visible. No MI model is included here.*

both the D^*Jet as well the Jet are created in the negative η region. This means that there is a lot of space for the parton showering. For the resolved processes the D^*Jet is created in the negative η region, whereas the Jet is created in the positive, which does not leave much space for parton showers in the $\mid \eta \mid < 1.5$ region.

8.3.1 The Effect of Multiple Interactions.

Figure 8.12 shows the multiplicity as a function of ϕ using MI-1. The direct contribution does not include any MI model but helps to show the change in the multiplicity in the transverse region: the resolved and charm excitation contributions have in this case a larger multiplicity. The regions toward and away are not much affected by the MI. Figure 8.13 shows a diagram where the D^*Jet and the Jet are created in the hard scattering and a second scattering occurs which populates the transverse region with aditional particles.

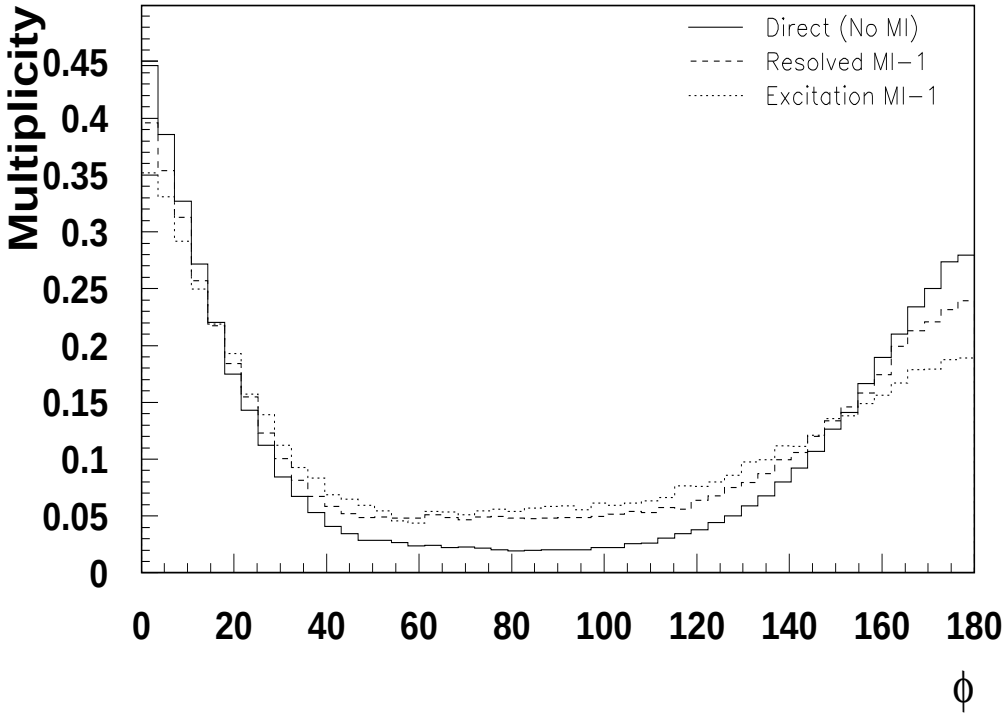

Figure 8.12: *Multiplicity as a function of ϕ for the direct, resolved and charm excitation components in $1D^*Jet + 1Jet$ events. The three regions: toward, away and transverse are clearly visible. MI-1 are included.*

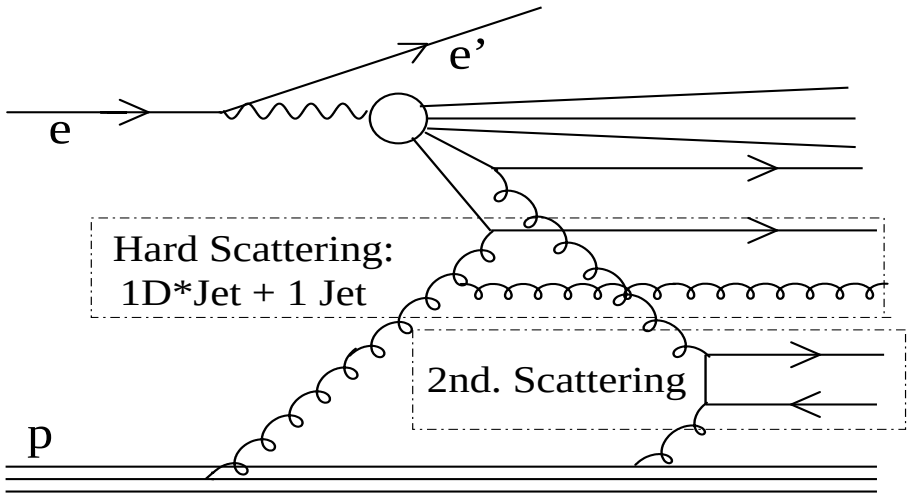

Figure 8.13: *The figure shows a charm excitation process where a second interaction occurs. The hard interaction is related with the multiplicity peaks in the toward and away regions, whereas the second interaction is reponsible of the enhancement in the transverse one.*

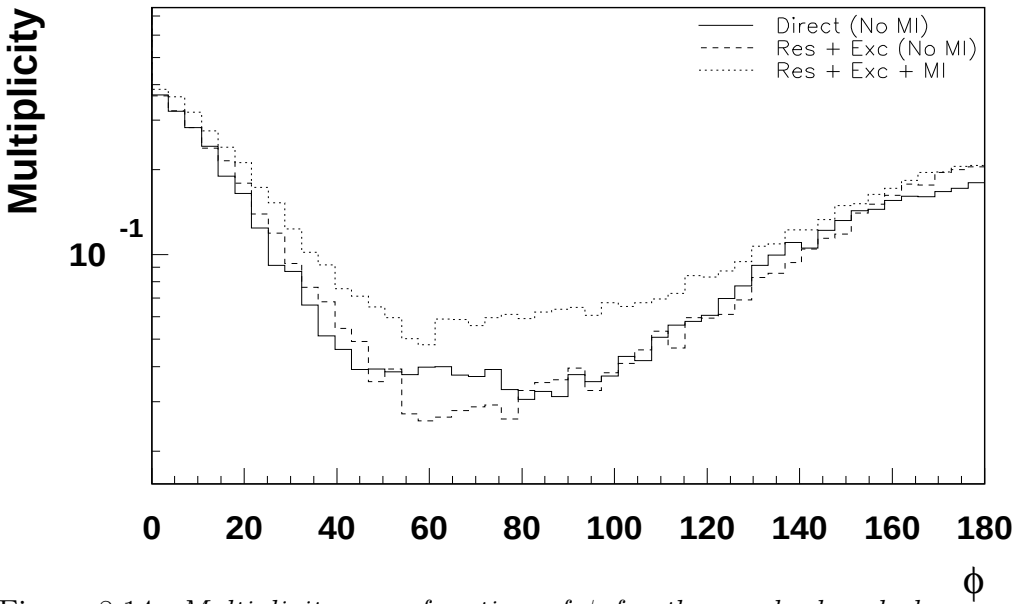

Figure 8.14: *Multiplicity as a function of ϕ for the resolved and charm excitation components and the direct one in $1D^*Jet + 1Jet$ events, including and not including MI.*

Since we are not able to measure experimentally the pure resolved and the charm excitation contributions separatelly it is useful to show these two contributions together. This is done in figure 8.14. The resolved components, resolved and charm excitation together, are 40% larger with MI.

Figure 8.15 shows the average multiplicity in the transverse region as a function of $P_t^{D^*}$ for resolved and charm excitation events, with and without MI. The enhancement is again large, about 40%.

8.3.2 Multiple Interaction. A New Comparison.

In this subsection we compare the different options of MI in PYTHIA. We use the MI default values and $1D^*Jet + 1Jet$ events for it. Since the cross section for charm excitation is larger than 15 times the resolved cross section for $1D^*Jet + 1Jet$ events, see table 8.2, we can neglect for simplicity the resolved component.

Figure 8.16 shows the multiplicity as a function of ϕ for charm excitation components. In this figure we show only three options: MI-1, all the events with the same MI probability, MI-2, same as MI-1 but with a continuos cut

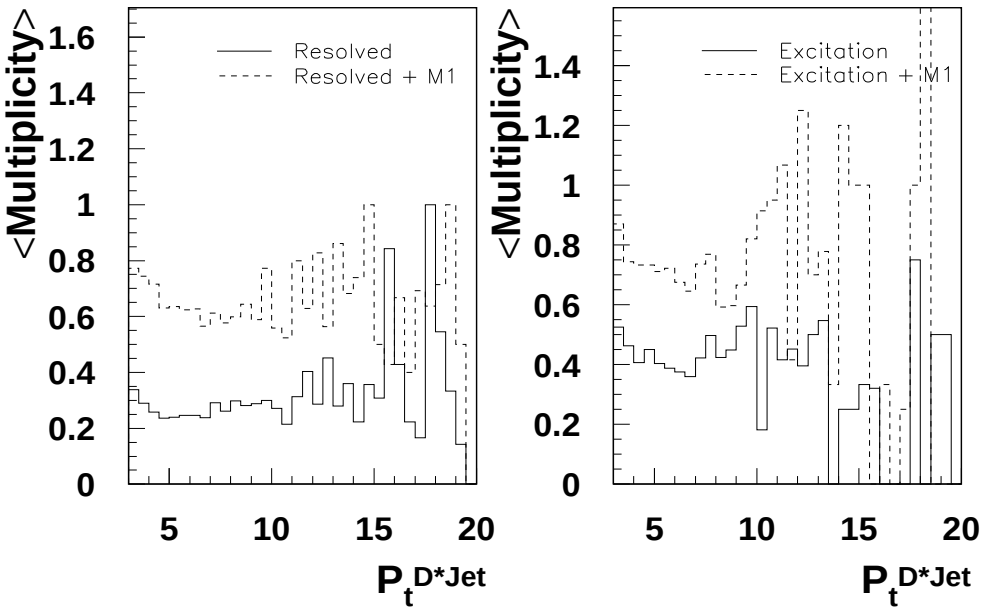

Figure 8.15: *Average multiplicity in the transverse region as a function of $P_t^{D^*}$ for the resolved and charm excitation components, including and not including MI.*

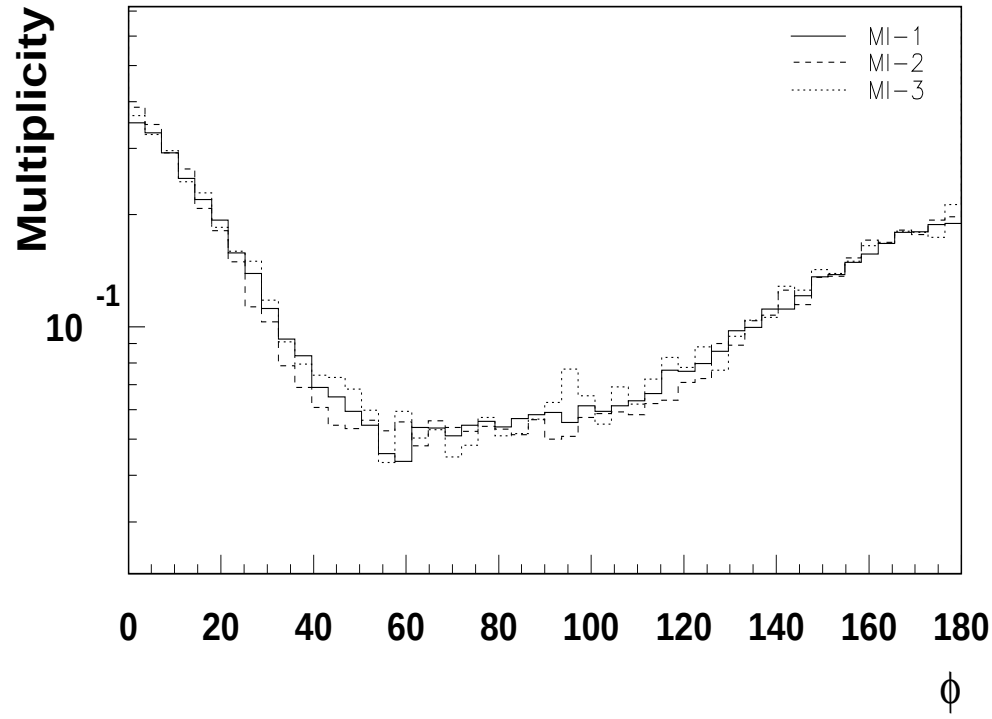

Figure 8.16: *Multiplicity as a function of ϕ for charm excitation components in $1D^*Jet$ events. The options MI-1, MI-2 and MI-3 (see table 2.1) are shown.*

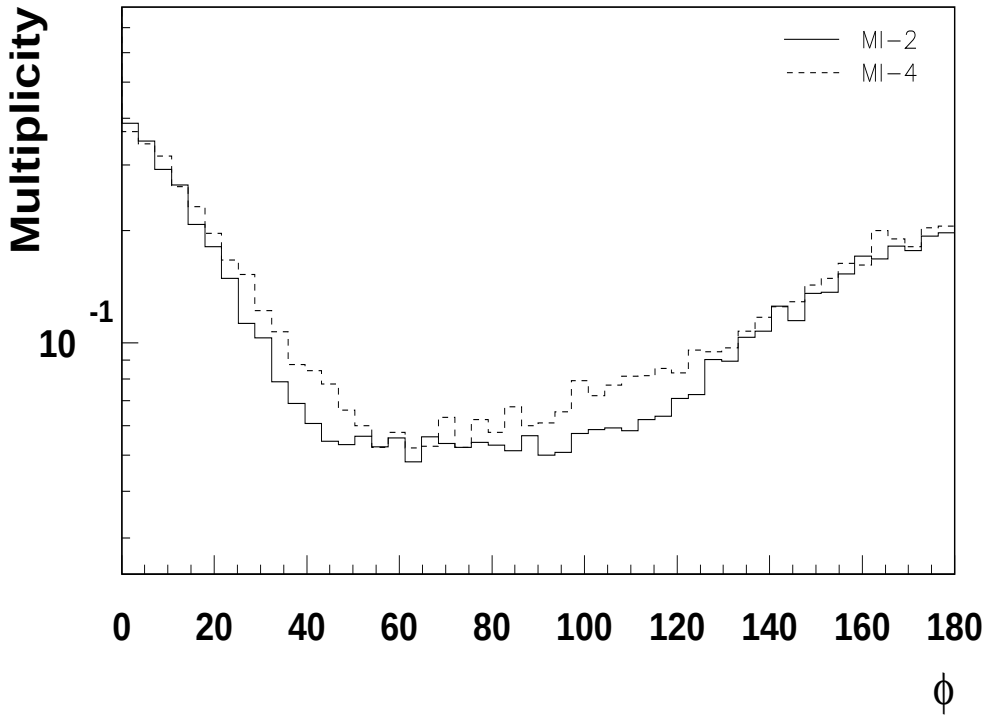

Figure 8.17: *Multiplicity as a function of ϕ for charm excitation components in $1D^*Jet$ events. The options MI-2 and MI-4 (see table 2.1) are compared.*

in $p_{\perp min}$, and MI-3, simple Gaussian matter distribution. We see that they do not differ much.

In figure 8.17, the options MI-4 and MI-2, as reference from figure 8.16 are compared. We see an enhancement on the borders of the toward-transverse and transverse-away regions, although in the regions $\mid \phi \mid < 30$ and $\mid \phi \mid > 130$, the most inner parts of the toward and away regions, remain without changes. As well as in chapter 7, we see that MI-4 predictions differ from the other options.

8.4 $1D^*Jet$ events.

Figure 8.18 shows the multiplicity as a function of ϕ in D^*Jet events for direct, resolved and charm excitation components. If we compare this figure

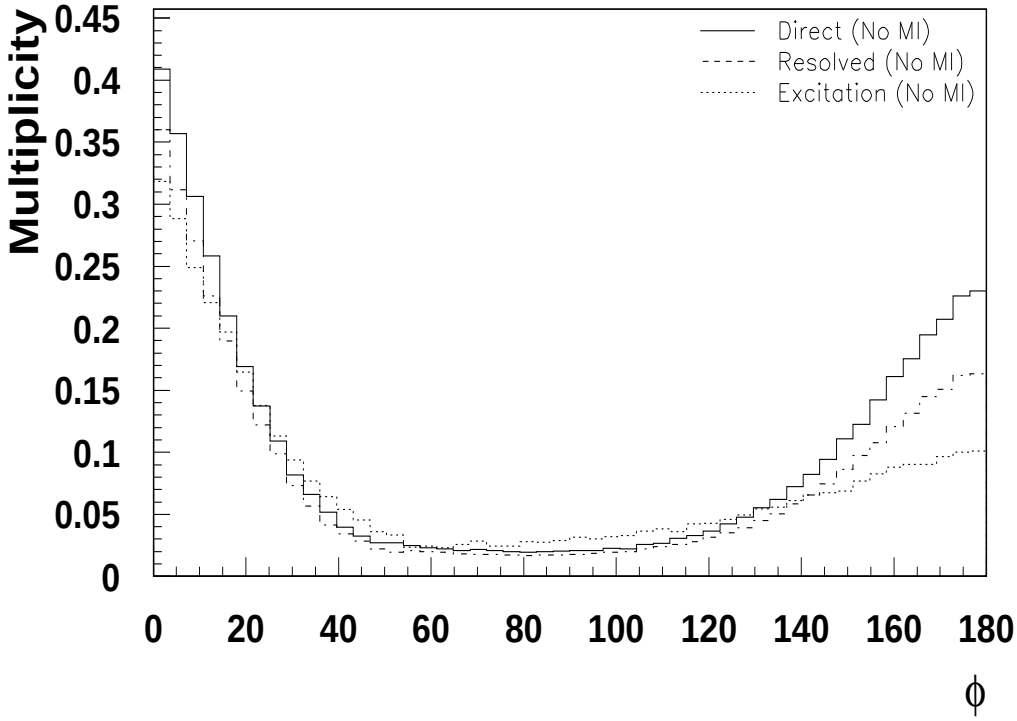

Figure 8.18: *Multiplicity as a function of ϕ for the direct, resolved and charm excitation components in $1D^*Jet$ events. No MI model is included here.*

with figure 8.11 in the toward and away regions, we see that the multiplicity in $1D^*Jet + 1Jet$ events is larger than for $1D^*Jet$ events. This can be understood since for $1D^*Jet + 1Jet$ events we have at least two jets, one in the toward region and the other one in the away region, with high transverse momenta whereas for $1D^*Jet$ we have many events with only one jet, the D^*Jet, and therefore the shape of the peaks are not so sharp as in the $1D^*Jet + 1Jet$ case. In the transverse region we see no significant changes.

In Figure 8.19 we present the multiplicity as a function of ϕ for D^*Jet events including MI, MI-1. As well as in the $1D^*Jet + 1Jet$ case the toward and away regions are not sensitive to MI, whereas the transverse region multiplicity is enhanced by a factor of 2 when including MI.

Figure 8.20 shows the comparison between multiplicities for the resolved components, i.e. resolved photon and charm excitation events, with and without MI. We see again the enhancement in the multiplicity, in this case about 30%, lower than for $1D^*Jet + 1Jet$ events.

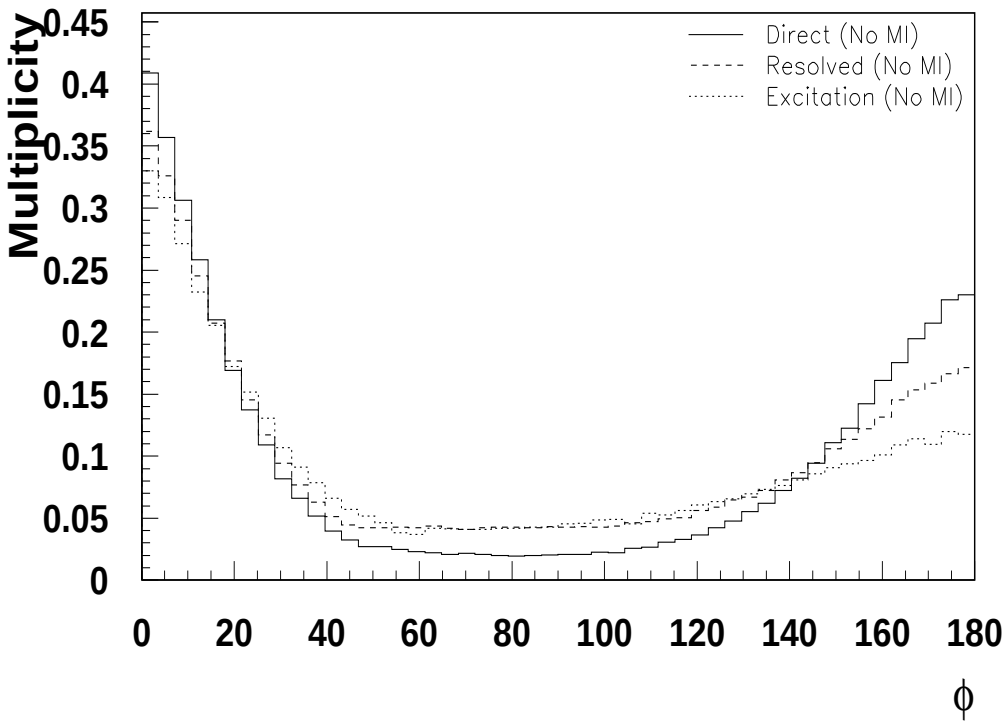

Figure 8.19: *Multiplicity as a function of ϕ for the direct, resolved and excitation components in $1D^*Jet$ events. MI are included.*

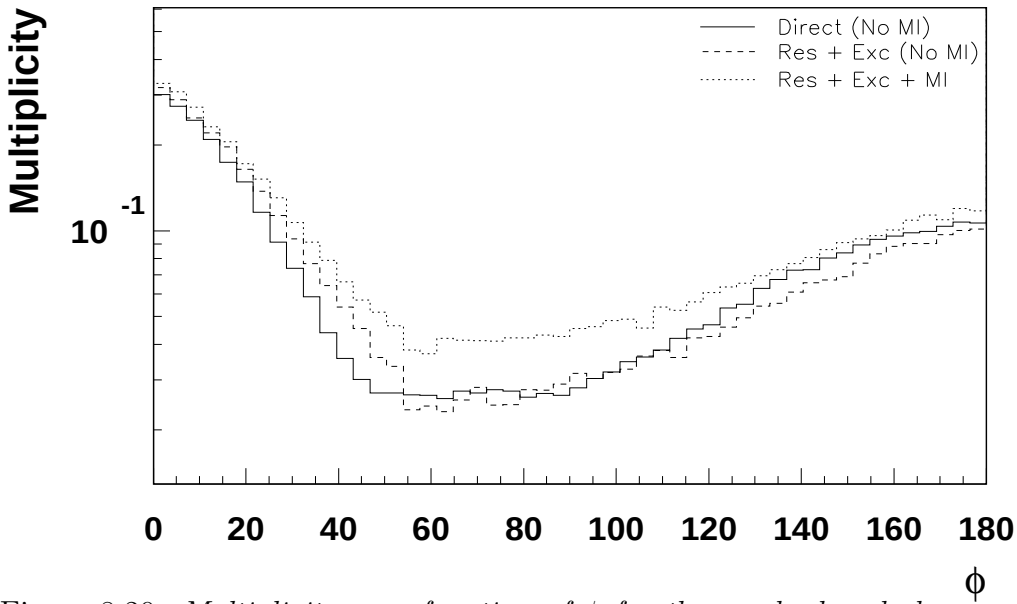

Figure 8.20: *Multiplicity as a function of ϕ for the resolved and charm excitation components and the direct one in D^*Jet events, including and not including MI.*

8.5 Multiplicity as a function of x_γ.

As we have seen, multiple interactions can take place in *ep* collisions when the remnants of the proton and of the photon interact. For this reason, in the study of MI at HERA the resolved photon and charm excitation processes are very important. In the theoretical overview we introduced x_γ in eq 2.17 which represents the momentum fraction of the photon entering in the hard interaction. In this section we present a study of the multiplicity as a function of x_γ.

Figure 8.21 shows the multiplicity as a function of ϕ in bins of x_γ for $1D^*Jet + 1Jet$ events. As in section 8.3.2 we only show the charm excitation component. We compare PYTHIA MI-2 with PYTHIA without MI. Although in the MI model the photon remnant is likely to interact with the proton remnant independently of x_γ, low values allow an enhancement of the multiplicity in the transverse region.

The explanation is that for x_γ values close to zero the photon remnant has a large energy. When it interacts with an incoming parton from the proton remnant, it has enough energy to be detected. If x_γ is close to one the photon remnant has not enough energy to be measured.

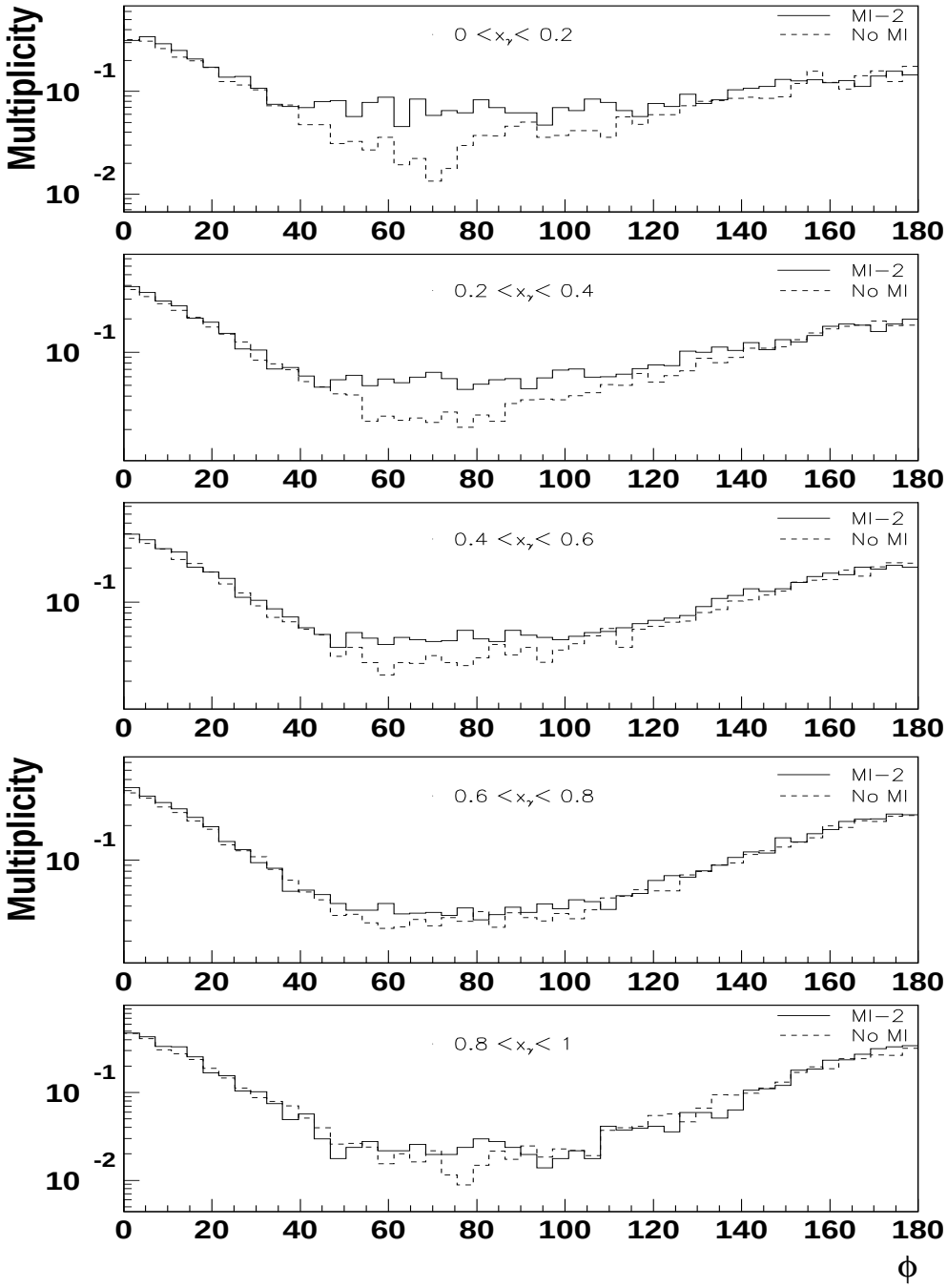

Figure 8.21: *Multiplicity as a function of ϕ in bins of x_γ for charm excitation in $1D^*Jet + 1Jet$ events. In this figure* PYTHIA *MI-2 and* PYTHIA *without MI are compared.*

No Multiple Interactions included			
Process	Cross Section(pb) Resolved	Cross Section(pb) Charm Excitation	Total
D^* in visible range	0.288	3.794	4.082
$1D^*Jet$	0.178	2.709	2.887
$1D^*Jet + 1Jet$	0.053	0.939	0.992
$1D^*Jet + 2Jet$	0.002	0.058	0.060

Table 8.2: *Cross Sections of some processes calculated with* PYTHIA *without MI.*

In this chapter we investigated MI in the D^* meson photoproduction. We compared the different options included in the MI model implemented in PYTHIA and we saw that the cross sections calculated with the double Gaussian matter distribution have interesting properties in the η distribution.

Finally, we saw that the transverse region can be very sensitive to MI, and that all the MI models predict an enhancement of the multiplicity in this region. The model where the hadron is represented as a warm core and a pion cloud surrounding it predicts a cross section which is different from the other models and this can be checked experimentally.

Chapter 9

Conclusions

The Monte Carlo event generators PYTHIA and RAPGAP were compared. We found that both generators agree reasonably well with each other in photoproduction after initial and final state parton shower at the 20% level.

The K_t and $CDF - CONE$ Jet algorithms and different Heavy Quark identification methods were studied. The cross sections calculated with these methods are similar at large transverse momentum, whereas small differences at small transverse momentum are observed, about 5%.

We studied the D^* Meson photoproduction, both in the inclusive D^* production and in D^* photoproduction associated with a jet. The cross sections predicted by PYTHIA agree fairly well with the measurements. However, significant differences are seen in the small $P_t^{D^*}$ region. The reason for this disagreement is not yet well understood. It could be related to the treatment of the heavy quark masses in excitation processes.

Effects coming from possible MI were investigated and cross sections of the D^* Meson photoproduction were calculated including multiple interactions. The predicted cross sections including MI increase, especially the one including a double Gaussian matter distribution for the proton, in the forward η_{Jet} region.

Finally, we investigated new and more clear signals for multiple interactions at hadron level. The multiplicity in the transverse region is very sensitive to MI, showing an enhancement of about 40%. This provides a clear signal, since the experimental errors in these measurements are expected to be small.

Appendix A

Main Parameters in RAPGAP and PYTHIA

Common RAPGAP Parameters

Parameter	Short description	Value	Remark
NFLA	Number of active flavours	4	
IQ2S	Definition of the hard scattering scale	5	$Q^2 + P_\perp^2 + m^2$
INPR	Proton structure function	1004046	CTEQ 5L

RAPGAP Parameters

Parameter	Short description	Direct Value	Resolved Value	Remark
IPRO	Hard subprocess selection	14	18	
PTCU	P^2_{tmin} for IPRO process	5	2	
NFQC	Num. of flavours used in QCD	3	4	
IHFL	Flavour produced	3	4	
INGA	Photon structure function	2	3005004	GRS-G LO

Table A.1: *Parameters used in* RAPGAP.

Common
PYTHIA Parameters

Parameter	Short description	Value	Remark
MSTP 32	Definition of the hard scattering scale	8	
MSTP 51	Proton structure function	4046	CTEQ 5L
MSTP 200	Flavour produced	4	

Parameter	Short description	Direct	Res.photon	Remark
MSTP 14	Structure of the incoming photon	0	1	
MSTP 55	Photon structure function	Not used	5003	GRV-G LO

PYTHIA Selected subprocesses: Direct

MSUB	Short description
84	$g + \gamma \to q + \bar{q}$

PYTHIA Selected subprocesses: Resolved Photon

MSUB	Short description
81	$q + \bar{q} \to Q + \bar{Q}$
82	$g + g \to Q + \bar{Q}$

PYTHIA Selected subprocesses: Charm Excitation

MSUB	Short description
11	$q_i + \bar{q}_j \to q_i + \bar{q}_j$
28	$q_i + g \to q_i + g$

Table A.2: *Parameters used in* PYTHIA. *This table is complemented with the tables 2.1 and 8.1*

Appendix B

Derivation of x_γ

In this section we present a derivation of the formula given in eq 2.17. We use the light-cone variable definitions (see [26]). Figure B.1 shows a resolved process with the relevant 4-momenta needed in the derivation

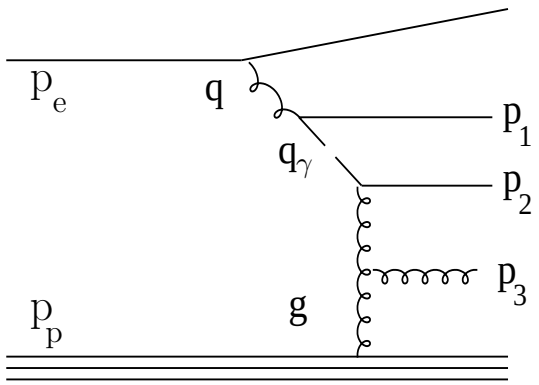

Figure B.1: *Resolved process with the relevant 4-momenta needed in the derivation*

If we neglect the masses of the proton and the electron, the 4-momenta can be written as:

$$p_p = (E_p, -Ep, \vec{0_t}) \quad \text{(B.1)}$$

$$p_e = (E_e, E_e, \vec{0_t}) \quad \text{(B.2)}$$

In light-cone variables this is:

$$p_p = (0, \frac{2Ep}{\sqrt{2}}, \vec{0_t}) \quad \text{(B.3)}$$

$$p_e = (\frac{2Ee}{\sqrt{2}}, 0, \vec{0_t}) \quad \text{(B.4)}$$

Here $\vec{0_t}$ is a two dimensional vector. In general we use a vector $\vec{q_t}$ as a two dimensional vector in the plane perpendicular to the ep collision.

We can write the 4-momenta q, q_γ and g using the light-cone variables as follows:

$$\vec{q} = (y \cdot P_e^+, \bar{y} \cdot P_p^-, \vec{q_t}) \quad \text{(B.5)}$$

$$q_\gamma = (x_\gamma \cdot y \cdot P_e^+, \bar{x_\gamma} \cdot \bar{y} \cdot P_p^-, \vec{q_{\gamma t}}) \quad \text{(B.6)}$$

$$g = (\bar{x_g} \cdot P_e^+, x_g \cdot P_p^-, \vec{g_t}) \quad \text{(B.7)}$$

In the high energy approximation $\bar{x_g}$ will be neglected.

For the two outgoing partons from the hard scattering we write:

$$p_2 = (E_2, -P_{2z}, \vec{P_{2t}}) \quad \text{(B.8)}$$

$$p_3 = (E_3, -P_{3z}, \vec{P_{3t}}) \quad \text{(B.9)}$$

Four momentum conservation gives (see figure B.1):

$$q_\gamma + g = p_2 + p_3 \quad \text{(B.10)}$$

Multiplying eq B.10 with p_p gives for the left side[1]:

$$p_p \cdot q_\gamma + p_p \cdot g \simeq P_p^- q_\gamma^+ = \frac{2Ep}{\sqrt{2}}\ x_\gamma\ y\ \frac{2Ee}{\sqrt{2}} \quad \text{(B.11)}$$

where we applied the high energy approximation and used light cone variables. The right side :

$$p_p \cdot p_2 + p_p \cdot p_3 = E_p E_2 - (E_p P_{2z}) \ + \\ + E_p E_3 - (E_p P_{3z}) = E_p \sum_{i=1}^{2} (E_i - P_{iz}) \quad \text{(B.12)}$$

[1]Remember that in light-cone variables a vector is written like: $v = (v^+, v^-, \vec{v_t})$ and that the 4-product is defined as: $v \cdot w = v^+ w^- + v^- w^+ - \vec{v_t}\vec{w_t}$.

Therefore, using B.11 and B.12:

$$2E_pE_e\ x_\gamma\ y = E_p \sum_{i=1}^{2} (E_i - P_{iz}) \tag{B.13}$$

Now, we work out the value of x_γ:

$$x_\gamma = \frac{\sum_{i=1}^{2} (E_i - P_{iz})}{2E_e\ y} \tag{B.14}$$

If $m \ll P_\perp$ the pseudo-rapidity is approximately the rapidity, which is defined as:

$$\eta \simeq y = \frac{1}{2} \ln \frac{E + P_z}{E - P_z} \tag{B.15}$$

From this equation:

$$e^{-\eta} = \sqrt{\frac{E - P_z}{E + P_z}} \tag{B.16}$$

If we multiply equation B.16 by $\sqrt{E - P_z}$ and use the E_t definition given in 2.18:

$$\sqrt{E^2 - P_z^2}\ e^{-\eta} = E - P_z = E_t\ e^{-\eta} \tag{B.17}$$

Using this last equation in B.14:

$$x_\gamma = \frac{\sum_{i=1}^{2} E_{ti}\ e^{\eta_i}}{2E_e\ y} \tag{B.18}$$

And this is the formula given in equation 2.17.

Bibliography

[1] Jung, Hannes, Comp. Phys. Commun. **86**, 147 (1995).

[2] Sjostrand, Torbjorn and Lonnblad, Leif and Mrenna, Stephen (2001).

[3] Flucke, Gero, *Photoproduction of D^* Mesons and D^* Mesons Associated with Jets at HERA.* H1, 2005.

[4] Halzen, Francis, *Quarks and Leptons: An introductory course in modern particle physics.* New York Wiley, 1984.

[5] Karlsson, Martin, *A Study of Parton Dynamics from Deep Inelastic Scattering Events Containing a Jet in the Forward Direction.* Lund University, 2002.

[6] Jung, Hannes, Mod. Phys. Lett. **A19**, 1 (2004).

[7] Jung, H., Phys. Rev. **D65**, 034015 (2002).

[8] Jung, H. and Salam, G. P., Eur. Phys. J. **C19**, 351 (2001).

[9] Sjostrand, T. and Skands, P. Z., Eur. Phys. J. **C39**, 129 (2005).

[10] Sjostrand, T. and Skands, P. Z., JHEP **03**, 053 (2004).

[11] Gwenlan, C., Acta Phys. Polon. **B33**, 3123 (2002).

[12] Aid, S. and others, Z. Phys. **C70**, 17 (1996).

[13] Adloff, C. and others, Eur. Phys. J. **C29**, 497 (2003).

[14] Jung, H., Comput. Phys. Commun. **143**, 100 (2002).

[15] Butterworth, J. M. and Couchman, J. P. and Cox, B. E. and Waugh, B. M., Comput. Phys. Commun. **153**, 85 (2003).

[16] Huth, John E. and others. Presented at Summer Study on High Energy Physics, Reaearch Directions for the Decade, Snowmass, CO, Jun 25 - Jul 13, 1990.

[17] Norrbin, E. and Sjostrand, T. (1999).

[18] Soper, Davison E. (1997).

[19] Seymour, M. H., Nucl. Phys. **B513**, 269 (1998).

[20] Wobisch, M. DESY-THESIS-2000-049.

[21] Angelini, L. and others, Phys. Lett. **B545**, 315 (2002).

[22] Abt, I. and others, Nucl. Instrum. Meth. **A386**, 310 (1997).

[23] Abt, I. and others, Nucl. Instrum. Meth. **A386**, 348 (1997).

[24] Bromley, J. and others. Prepared for Workshop on Future Physics at HERA (Preceded by meetings 25-26 Sep 1995 and 7-9 Feb 1996 at DESY), Hamburg, Germany, 30-31 May 1996.

[25] Affolder, T. and others, Phys. Rev. **D65**, 092002 (2002).

[26] Collins, John C. (1997).

Acknowledgments:

I would like to thank Prof.Dr.Beate Naroska and Dr.Carsten Niebuhr for the opportunity to study and work at DESY and to perform this thesis. I have to say that this last year was really challenging and I enjoy it very much working here.

I want to thank very especially Dr.Hannes Jung, my supervisor, for his support, help and all what I learnt working with him and of course for his patience. It was very nice to go to the Blaue Blume with him and all the group.

Very important in this last year was also the people in our room because they made of it a very good place to work: Axel, Nina and Jan (only God knows how many Doppel-Keks and other sweets we ate). I want also to thank Gero for all the discussions we had about D^* photoproduction. I do not forget the people at the mondays meetings "Physics and cookies": Svetlana, Adrian, Angela, Kaloyan, Kristin...

Ich danke ganz besonders Imke und Dominik, die immer bereit sind, mir zu helfen wie auch Martin und Yvonne, die ich sehr hoch schätze.

Naturalment estic molt agraït de tot cor a la meva familia, Maria, Luis i Selma (sense cap mena d'ordre), aixi com l'Alex, per estar sempre amb mi, escoltar-me i ajudar-me sigui quina sigui l'empresa esbojarrada que emprengui (encara que no sempre molt convençuts).

Finally I want to thank the DAAD and "la Caixa" for their financial support and the DAAD-Freundeskreis for all the activities they organize for the scholars in Hamburg.